IEEE Access
Multidisciplinary | Rapid Review | Open Access Journal

Received February 1, 2019, accepted March 13, 2019, date of publication March 18, 2019, date of current version April 5, 2019.

*Digital Object Identifier 10.1109/ACCESS.2019.2905856*

# Novel Non-Linear Transient Path Energy Method for the Analytical Analysis of the Non-Periodic and Non-Linear Dynamics of Electrical Machines in the Time Domain

**NIKITA GABDULLIN, (Member, IEEE), AND JONG-SUK RO**
Department of Electronic and Electrical Engineering, Chung-Ang University, Seoul 06974, South Korea

Corresponding author: Jong-Suk Ro (jongsukro@gmail.com)

This research was supported by the Basic Science Research Program through the National Research Foundation of Korea funded by the Ministry of Education (2016R1D1A1B01008058), by Korea Western Power Generation Co., Ltd., and by the Korea Electric Power Corporation (Grant R17XA05-30).

**ABSTRACT** This paper proposes a novel analytical method for the analysis of the dynamics of electrical machines. The method is applied to the analysis of complex permanent magnet (PM)-type magnetic contactors (MCs), which exhibit strong magnetic non-linearities and a high portion of stray and leakage magnetic fluxes. The latter means that the analysis of PM-type MCs using traditional magnetic equivalent circuit (MEC) methods is impossible, thus requiring computationally expensive and time-consuming finite element analysis (FEA). To overcome the limitations of traditional MECs, the magnetic field distribution in PM-type MC is studied in great detail, and a novel non-linear dynamic MEC (ND-MEC) method is proposed. The accuracy of the ND-MEC method is comparable to that of FEA which is achieved by accounting for non-linear effects and dynamic changes in the magnetic flux distribution using a novel stray path elliptical function. Furthermore, the applicability of the ND-MEC is extended to the time domain by combining it with the time difference method (TDM). The complete method, referred to as the non-linear transient path energy method (NT-PEM), combines the ND-MEC, TDM, and a path energy method for the calculation of electromagnetic forces. The validity of the NT-PEM is verified by comparing it with 3D FEA and experimental results obtained from a PM-type MC prototype. The NT-PEM is a fast and inexpensive alternative to FEA, which is particularly advantageous when many designs must be analyzed and optimized while reducing analysis costs. The proposed method can also be applied to the analysis of emerging technologies dealing with multiphysics coupled problems, as in the case of smart materials.

**INDEX TERMS** Magnetic contactor, magnetic equivalent circuit (MEC), nonlinear dynamics, permanent magnets, stray flux modeling.

## I. INTRODUCTION

With the increase in computational speeds and advances in numerical methods, analysis techniques such as the finite element method (FEM) have become indispensable and powerful analysis tools [1]–[4]. However, even with the use of high-performance computers, analyzing a large number of models or running optimization algorithms substantially increases the overall analysis time [5], [6]. Because the FEM divides a continuous model into a finite number of nodes and elements via meshing, the number of equations increases dramatically, potentially leading to significant computational time [7]. Furthermore, structural and material non-linearities can dramatically increase the number of iteration steps required for the analysis to converge [8]. In addition, finite element analysis (FEA) has several disadvantages compared to analytical models [9], [10]. For instance, with the increasing complexity of a model, the mutual influence of various design parameters becomes difficult to estimate [11]. Therefore, the high accuracy of the method comes at expense of time and the loss of certainty in result interpretation.

The disadvantages of the FEM mean that accurate analytical techniques are particularly advantageous in the early design stages when many different designs and design

The associate editor coordinating the review of this manuscript and approving it for publication was Bing Li.

parameters are considered [12], [13]. A common and reliable method used for this purpose is the application of equivalent electric circuit of magnetic circuit of electrical machines, or magnetic equivalent circuit (MEC) [14], [15]. Other types of equivalent circuits, such as mechanical or thermal, are also very useful for modeling kinematics or temperature distribution [16]. However, these approaches are usually considered less accurate compared to FEM due to several inherent limitations. First, the MEC models are essentially one-dimensional (1D) because the currents, or fluxes in the magnetic analogy, correspond only to the normal components of the corresponding three-dimensional (3D) electromagnetic field vectors. Second, capturing the non-linear properties of materials and their complex geometries is usually extremely difficult. Third, the magnetic field distribution is heavily simplified because the flux paths are restricted to a limited number of conductive branches for each of which the flux is constant. Finally, fluxes that deviate from the flux guide regions are typically ignored.

Nevertheless, MEC models can be extremely useful in the initial design stages due to their simplicity, their reduced computational time, the transparency of the effects of different parameters, and their compatibility with optimization algorithms [17]. However, the application of the MEC method to actuator designs with complex geometry is impossible due to the complicated flux distribution, which cannot be captured by traditional MECs [18], [19]. Moreover, the strong magnetic fields, which lead to the magnetic saturation of the actuator's core, can increase the error of traditional MECs even further due to associated non-linear effects [20]. Consequently, time-consuming FEA is most often used for the analysis of geometrically complex models where non-linearity is high due to the magnetic saturation effects [21], [22].

To address these problems and improve the accuracy of the MEC method, this paper proposes a novel non-linear dynamic MEC (ND-MEC), which can account for changes in MEC parameters arising from the saturation of the core and the motion of the actuator's armature. The structure of the proposed ND-MEC is rather simple, which ensures rapid analysis because computational time is proportional to circuit complexity [23]. In order to account for core saturation, the ND-MEC incorporates an iterative algorithm for the correction of varying core permeability using a $\mu_r(H)$ rational function that approximates $B$–$H$ material experimental data and displacement-dependent parameters that change according to the dynamic behavior of the actuator. Moreover, the introduction of position-dependent stray path reluctances allows the 3D paths of stray fluxes to be modeled with high accuracy using a novel elliptical function proposed in this study. The proposed ND-MEC method maintains the simplicity of traditional MECs and combines it with innovative advantageous features leading to substantially shorter computational time compared to 3D FEA.

The proposed ND-MEC method is used to analyze a 220V/85AF magnetic contactor (MC) with a complex 3D field distribution that has a considerable portion of its total flux deviating from the main flux path [24]. This high flux leakage compared to other types of electrical machines, especially rotating electrical machines, is a consequence of the large air gaps in the MC. When the MC is in an open state, large working gaps, which are part of the main magnetic flux path, are a necessary design feature to ensure the reliable breaking of the current in a controlled circuit, decreasing the chances of arcs and contact welding. This flux leakage means that the analysis of MCs using the MEC method is substantially more complex than, for instance, that of interior permanent magnet (IPM) motors, which have been studied extensively in recent years [19], [25], [26].

The ND-MEC method proposed in this paper is also combined with the time-difference method (TDM), allowing the complete dynamics of the studied MC to be evaluated [27]. This combined analytical method for the evaluation of the dynamics of electrical machines, referred to as the non-linear transient path energy method (NT-PEM) in this paper, is shown to be extremely fast and accurate. The method owes its name to the way in which the contribution of different flux paths is considered, as discussed in detail in Section VI. The path-dependent effects and energies associated with different flux paths in the target MC that are considered by the NT-PEM significantly influence traditional design parameters, such as the magnetic circuit saturation conditions. Furthermore, the influence of path energies extends further, affecting the overall performance of the MC, including coil currents, electromagnetic force, armature displacement or rotor positions. The NT-PEM can be employed in the design and analysis of a variety of electrical machines and holds the potential for further generalization due to its multiphysics capabilities and applicability in multidisciplinary research [28], [29]. The validity of the proposed method is verified by comparing its results with those obtained from 3D FEA using the commercial software tool JMAG and experimental results obtained from an MC prototype.

## II. ANALYSIS OF AN MC WITH A PERMANENT MAGNET

### A. OPERATING PRINCIPLES OF THE 220V/85AF MC

This paper studies the dynamic behavior of the 220V/85AF MC shown in Fig. 1. MCs are an essential component of the switchgear in electrical systems, employed along with other circuit breakers and fuses to ensure reliable operation and protect the system from adverse malfunctions or damage. MCs are primarily used to switch power circuits in low-power electrical machines, such as electric motors, lighting and heating circuits, and capacitor banks. The switching procedure is executed by the actuator in the MC, which separates the moving contacts from the stationary contacts, as shown in Figs. 1 (b) and (c). Originally, a spring mechanism was used for this purpose due to its low cost, but a mechanical spring is unreliable due to its high risk of malfunction.

Solenoid actuator technology has been proposed as a solution to the problems encountered by spring-type MCs. A solenoid-type MC offers numerous advantages, including

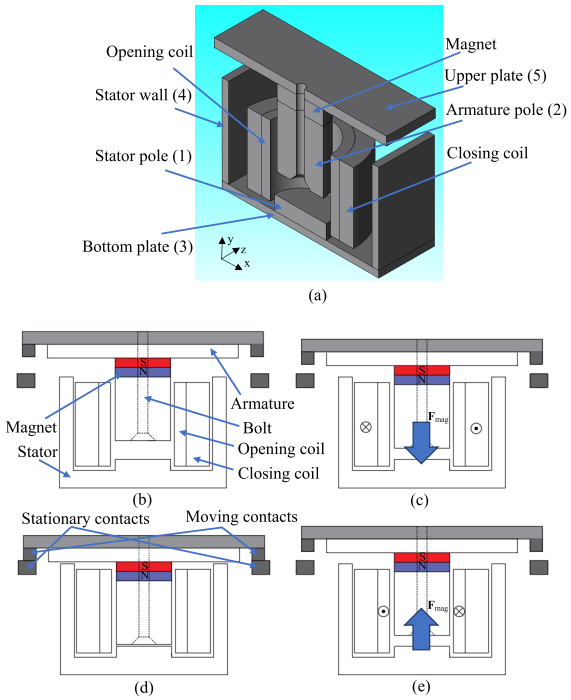


**FIGURE 1.** (a) Magnetic circuit of the studied MC. The numbers in parentheses correspond to the associated regions in the ND-MEC model. Operating regimes of the MC: (b) open state, (c) closing, (d) closed state, and (e) opening.

remote control and greater reliability. However, solenoid-type MCs consume more energy, decreasing their efficiency and increasing overall energy loss and heat generation. They are also subject to more mechanical vibration and noise because solenoid-type MCs need to be energized when they are in a closed state. The holding force in a closed state is produced by periodic AC current, so the electromagnetic force oscillates, leading to vibrations that increase the probability of contact welding, decreasing the reliability of the MC.

Permanent magnet- (PM-)type MCs have been proven to be able to overcome the drawbacks of solenoid-type MCs [24]. The closed state of a PM-type MC is maintained by the attractive electromagnetic force between the magnet and the stator core. This force is produced by the magnet, so no electric current is required when the MC is in a closed state, meaning that PM-type MCs are significantly more energy efficient and eco-friendly compared to solenoid-type MCs. Furthermore, the constant, non-oscillating holding force produces no vibrations, preventing contact welding. In addition, this type of MC does not require core lamination and has a mechanical guiding structure. The former feature reduces manufacturing costs, and the latter increases the mechanical stability.

As shown in Figs. 1 (a) and (b), the flux guide of the studied MC consists of a stator, an armature, opening and closing coils, and a magnet. Four operating regimes characterize the MC: closing, maintaining the closed state, opening, and maintaining the open state. Fig. 1 (b) shows that, in an open state, the armature is located at its maximum distance from the stator and the moving contacts are not in contact with the stationary ones. When the closing coil is connected to the voltage source, the magnetic field produced by the induced current aligns with the PM's magnetic field, resulting in an attractive electromagnetic force (Fig. 1 (c)). When the armature reaches the stator and the air gap is minimized, the closing coil disconnects from the voltage source and a closed state is maintained by the holding force produced by the PM. In closed state, the moving and stationary contacts are connected, allowing the flow of current within the controlled circuit, as shown in Fig. 1 (d). As discussed in further detail in Section V, the opening of the MC is initiated by energizing the opening coil using a capacitor that is charged during the closing operation. The direction of the magnetic field produced by the opening coil current is opposite to that of the PM magnetic field, resulting in electromagnetic repulsion (Fig. 1 (e)). The opening operation is assisted by a mechanical spring to ensure the rapid switching of the controlled current (not shown in Fig. 1). At the end of opening operation, the MC is in an open state, ready for the next closing operation.

### B. STRUCTURE OF THE PROPOSED ND-MEC

The stator and armature, which are shown in detail in Fig. 1(a), form the magnetic flux guide of the MC. To simplify the discussion of the model, the following notation system is utilized: the width of the $i$-th region in the $x$-direction is denoted as $a_i$, its height in the $y$-direction is $h_i$, and the length in the $z$-direction is $l_i$. As shown in Fig. 1 (a), the stator core consists of a pole (region 1), a bottom plate (region 3), and walls (region 4). The armature consists of a central pole (region 2), an NdFeB magnet, and an upper plate (region 5). There is one gap in the center of the contactor between the stator and armature poles, and two gaps, one on each side, between the stator walls and the upper plate of the armature. There is a non-magnetic bolt located at the center of the armature used for positioning the magnet (Fig. 1 (b)). The regions with different geometries and/or properties are represented by different reluctances in the ND-MEC.

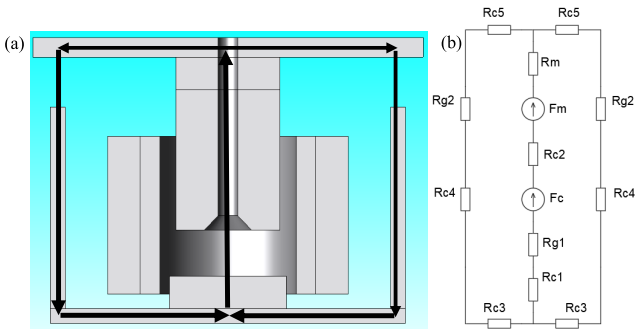


**FIGURE 2.** (a) Path of the main magnetic flux of the MC. (b) Conventional MEC considering only the main magnetic flux path of the MC.

Traditional MECs typically consider only the main flux paths, as shown in Fig. 2. Because the main paths only include the core regions and the shortest air gap paths, their use

in actuator analysis with a complicated 3D flux distribution can lead to considerable error. This can be illustrated by the comparison between the analysis using an equivalent circuit in Fig. 2 (b) and FEA results. In the equivalent circuit, the magnetomotive force (mmf) $F_c$ produced by the coils is represented by the voltage source. In a similar manner, the PM is modeled as the mmf source $F_m$ with a series reluctance [23], [30]. All of the core and air gap regions are represented by the reluctances $R_i$ and $R_{gi}$, respectively. The parameters of this circuit can be represented by

$$R_i = \frac{l_i}{\mu_0 \mu_{ri} A_i} \tag{1}$$

$$F_c = N_c i_c \tag{2}$$

$$F_m = H_c h_m \tag{3}$$

where $l_i$ is the flux path length in the $i$-th reluctance (m), $A_i$ is its cross-section area ($m^2$), $\mu$ is the permeability of free air (H/m), $\mu_{ri}$ is the relative permeability, $N_c$ is the number of coil turns,$i_c$ is the coil current (A), $H_c$ is the coercive force of the magnet (A/m), and $h_m$ is the height of the magnet (m). In order to demonstrate the inaccuracy of the main path circuit, the problem is solved using both a main-path MEC and the FEA software JMAG. For this experiment, the coil parameters are $i_c = 2.5$ A and $N_c = 2000$, and the analysis is conducted for both the open and closed state of the MC, i.e., when the air gaps are at their maximum and minimum value, respectively.

**TABLE 1. Comparison of the calculated magnetic flux density (*B*, T) in various regions of the MC using the FEA and MEC shown in Fig. 2, which takes into account only the main flux path of the MC.**

| Reluctance | *B*, T (FEA) | *B*, T (MEC) | *B*, T (FEA) | *B*, T (MEC) |
|---|---|---|---|---|
| State | Closed state | | Open state | |
| Main gap *Rg1* | 2.17 | 1.24 | 0.56 | 0.42 |
| Side gap *Rg2* | 0.73 | 2.55 | 0.22 | 1.1 |
| Stator pole *Rc1* | 1.6 | 0.78 | 0.76 | 0.33 |
| Armature pole *Rc2* | 2.1 | 1.03 | 1.13 | 0.44 |
| Stator plate *Rc3* | 1.8 | 2.23 | 1.28 | 0.95 |
| Stator wall *Rc4* | 1.67 | 2.23 | 0.85 | 0.95 |
| Armature plate *Rc5* | 1.17 | 1.03 | 0.7 | 0.84 |

The analysis results shown in Table 1 illustrate that the accuracy of this MEC is not acceptable for MC design. Therefore, further analysis is conducted on an MEC that includes additional reluctances that account for the paths that fluxes take deviating away from the main path, i.e., the complete ND-MEC proposed in this research (Fig. 3). Multiple stray and leakage flux path reluctances are included in the circuit, such as the magnet leakage reluctance $R_{ms}$, the main air gap stray path reluctance $R_{g1s}$, the coil to stator stray path reluctance $R_{c1s}$, the coil to the armature stray-path reluctance $R_{c2s}$, the side gap stray path reluctance $R_{g2s}$, and the $R_{g2f}$ reluctance, which accounts for the 3D effects of the magnetic distribution near the side gap regions. Core regions $R_{c1}$–$R_{c5}$ are divided into multiple sub-regions, providing points of

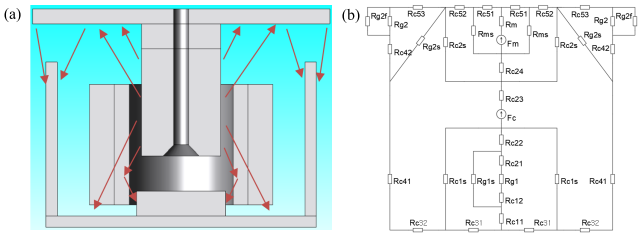


**FIGURE 3. (a) Directions of the stray magnetic fluxes in the MC. (b) ND-MEC proposed in this research that includes additional reluctances for modeling stray and leakage magnetic fluxes in the MC.**

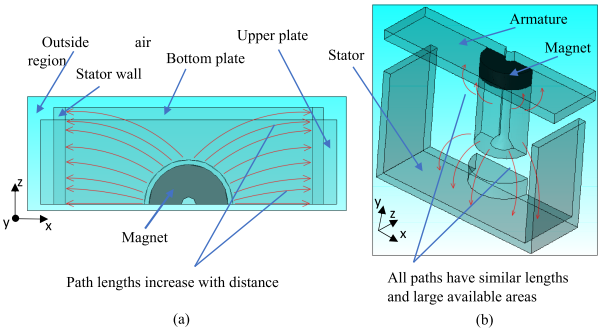


**FIGURE 4. (a) Top view of the MC showing the high-reluctance stray paths between the center and walls. (b) Low-reluctance paths between the central section and upper and bottom plates.**

connection for stray path branches with the flux guide. Reluctance $R_{c21}$ accounts for changes in the core cross-sectional area due to the non-magnetic bolt used to position the magnet. It should be noted that the geometry of contactor's core has a significant effect on the ND-MEC structure. For instance, the coil flux could be expected to flow directly to the stator walls (the $R_{c41}$–$R_{c42}$ region). However, because the central part of the armature is cylindrical and the stator walls are rectangular, the paths between most of the points on the cylinder and those located on the stator walls are relatively long, making these paths less preferable (see Fig. 4 (a)). On the other hand, the top and bottom rectangular plates provide a considerable area for the flux to pass through, rendering the associated paths extremely conductive (Fig. 4 (b)). Hence, the geometry of the MC should be considered carefully when designing an ND-MEC model.

The analysis results shown in Table 1 illustrate that the accuracy of this MEC is not acceptable for MC design. Evaluating the parameters of the ND-MEC in Fig. 3 is more complicated compared to the main flux MEC in Fig. 2 for a number of reasons. Stray paths pass through air regions, making the calculation of the associated reluctances challenging, while most of the reluctances in Fig. 3, including the stray path reluctances, vary with the position of the armature due to changes in the size of the air gaps. In addition, changes in the supply current lead to changes in the core steel $B$–$H$ curve operating point and the permeability of the core reluctances. In order to address these problems, this paper presents an iterative algorithm that takes core non-linear properties into

account and proposes a novel method that uses an elliptical function to evaluate the stray path reluctances is proposed in this paper.

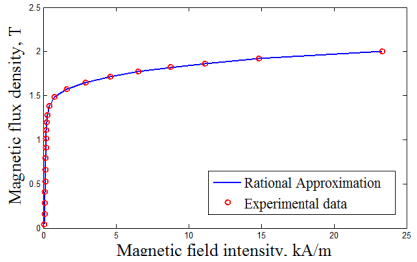


**FIGURE 5.** Comparison of the experimental *B–H* curve and rational function approximation.

## III. DETERMINATION OF THE RELUCTANCES IN THE ND-MEC

### A. CONSIDERATION OF NON-LINEAR EFFECTS IN CORE REGIONS

While handling material non-linearities is usually considered a challenge for a traditional MEC, new approaches have been proposed in recent years [31], [32]. Many authors have proposed utilizing curve-fitting techniques to obtain a polynomial representation of the $B(H)$ relation, whereas peacewise approximation and other types of interpolation have also been employed [25], [33]. In this paper, a recently proposed method utilizing the rational function $\mu_r(H)$ is used to calculate the relative permeability at every step of the iterative procedure shown in Fig. 5 [34]. This rational function allows the representation of a discrete dataset with a continuous function constructed of the sum of the fractions of low-order polynomials. For the *B–H* dataset of the steel used in this study, the function is obtained from (4) and (5) [shown at the bottom of this page]

$$B = \mu_0 \mu_r(H) \cdot H \tag{4}$$

where $H$ is the magnetic field strength (A/m), and $B$ is the magnetic flux density (T). As shown in Fig. 5, the smooth function $B(H)$, obtained by combining (4) and (5), fits the experimental data extremely closely. The root mean square (RMS) error in the flux density is only $4 \cdot 10^{-4}$ T. This proves the applicability of the proposed method in modeling the non-linear properties of the core material. Function (5) is used to correct the permeability values for the core reluctances *Rc11–Rc53* at every step of the iterative procedure described below.

The proposed iterative algorithm for core permeability correction shown in Fig. 6 has one initial step and a varying number of following iteration steps. First, the circuit equations are solved using the initial core permeability. In the first

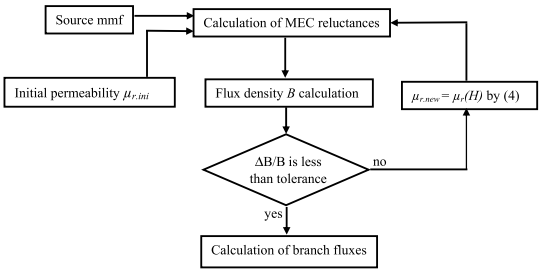


**FIGURE 6.** The proposed iterative algorithm for working point evaluation on the non-linear *B–H* curve via core permeability correction.

iterative step, the initial value $\mu_{r.ini} = 4000$ is used. For the obtained fluxes, the field intensity $H$ is calculated using (5), which is further used to calculate updated values for $\mu_r$, thus adjusting the core reluctances. The circuit equations are then solved again for the updated circuit parameters, and the relative change in flux density $\Delta B/B$ is calculated for every core reluctance element. This procedure repeats until all reluctance elements satisfy a desired tolerance. The updated values of the field intensity $H_i$ for all core reluctances are calculated using (6).

$$H_i = \frac{\Phi_i}{\mu_0 \mu_{ri} A_i} \tag{6}$$

where $\Phi_i$ is the magnetic flux in the *i-th* branch (Wb).

### B. DETERMINATION OF THE RELUCTANCES FOR THE MAIN FLUX PATH OF THE ND-MEC

The main flux reluctances were previously mentioned in Section II. It should be stressed that the main assumption for the main flux path is that the flux does not deviate from strictly horizontal or vertical paths, as shown in Fig. 2 (a). Therefore, the main path reluctances conduct fluxes that primarily have only one component normal to the flux guide surface. This is particularly important for air regions because any change in the flux and energy stored in these reluctances contributes fully to the output force. However, this is not true for the energy stored in the stray path reluctances. This will be discussed in detail in Section VI.

Only two reluctances in the circuit correspond to the main path air reluctances: *Rg1* and *Rg2*. They can be expressed as

$$R_{g1} = \frac{l_{g1min} + x}{\mu_0 A_1} = \frac{l_{g1min} + x}{\pi r_1^2 \mu_0} \tag{7}$$

$$R_{g2} = \frac{l_{g2min} + x}{\mu_0 A_4} = \frac{l_{g2min} + x}{a_4 l_{z4} \mu_0} \tag{8}$$

where $l_{g1min}$ and $l_{g2min}$ are main and side air gap lengths in a closed state (m), $r_1$ is the radius of the cylindrical armature core section (m), $a_4$ and $l_{z4}$ are the width and length of the

$$\mu_r(H) = \frac{1}{\mu_0}\left(\mu_0 + \frac{0.86}{H + 18696.5} + \frac{0.53}{H + 209.1} + \frac{0.8\,(H + 56.3)}{(H + 4.5)^2 + 80.7^2} + \frac{0.13\,(H - 69.2)}{(H - 29.6)^2 + 27.2^2}\right) \tag{5}$$

stator wall, respectively (m), and $x$ is the position of the armature (m). Therefore, the sums in the numerators in (7) and (8) are the total lengths of the corresponding air gaps. Because it is assumed that the flux does not deviate from a straight path, areas $A_1$ and $A_4$ correspond to the geometry of the flux guide sections adjacent to the air gaps.

### C. A NOVEL METHOD FOR THE CALCULATION OF STRAY PATH RELUCTANCES

While leakage flux modeling is important for all electrical machines, it is essential in this study due to the considerable proportion of the total flux that deviates from the main path of the MC. All of the flux paths that do not coincide with the main path pass through air regions and are longer than the main paths. This leads to a common assumption that the reluctances associated with these paths are large and that leakage fluxes are much lower than the main flux. However, this is not the case in this type of MC. This can be illustrated by analyzing the difference between the traditional MEC shown in Fig. 2(b) and the proposed ND-MEC in Fig. 3(b). The reluctances added in Fig. 3(b) account for the paths that the fluxes take in regions where the reluctance of the main path is expected to be comparable with the stray path reluctances. It should be mentioned that the flux distribution and the tendency of the flux to deviate from the main path changes with armature motion. Therefore, the reluctances of the stray paths change with the position of the armature, greatly complicating the analysis. This problem is addressed using the novel technique discussed below.

In general, the calculation of stray path reluctances is complicated because the path lengths and associated cross-sectional areas are unknown. Therefore, certain assumptions need to be made. A common assumption used for stray flux modeling utilizes the concept of flux tubes [35]–[37]. Flux tubes permeate the entire space, are finite in number, and conduct constant magnetic fluxes, just as the MEC branches normally do. The geometry of the flux tubes determines the reluctances of associated regions [38]. In this context, it is important that the main air path flux tubes do not bend, meaning that the associated fluxes have zero tangential components. However, leakage flux tubes do bend upon leaving and re-entering the flux guide regions, and the shapes of the associated flux tubes can vary. It has previously been proposed that stray fluxes should be treated as fluxes that follow straight lines or circular paths, or a combination of both [39], [40]. These approaches have shown some success in stray path modeling. However, these approaches require air regions to be relatively small compared with the size of the flux guide core, which is not the case for the studied MC. This leads to the "stretching" of field lines along the length of the air gaps, resulting in the inapplicability of the above methods.

The novel approach proposed in this paper aims to provide a generalized approach for stray path modeling and the calculation of related reluctances. First, the areas that contribute to the stray flux reluctance are divided into a finite subset of areas. This is done by introducing the parameter $a_s$ [40],

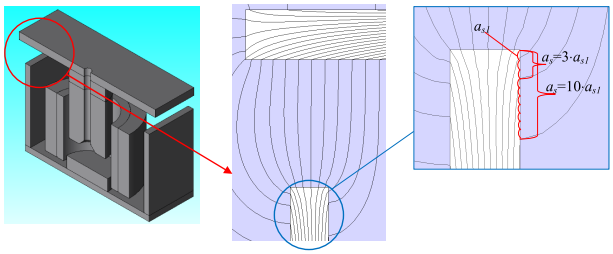


**FIGURE 7.** 2D magnetic field lines near the side air gap region of the contactor; the inset illustrates the method for estimating the flux tube parameters.

which can be determined based on step $a_{s1}$ and the position of the center of a flux tube, as shown in Fig. 7. For each flux tube, the length of the path is calculated using the elliptical function described below. This avoids the necessity of guessing the shape of the path. The application of the elliptical function is possible because magnetic field lines tend to follow elliptical paths [41], [42]. When field lines are modeled as elliptical paths, two extreme cases are possible: straight-line paths, when the focal distance of the ellipse tends towards infinity, and circles, when the focal distance approaches zero. While the calculation of reluctances based on straight lines and circular arcs is more straightforward, the elliptical arc approach allows for the path length of arbitrary stray fluxes to be determined thereby avoiding the limitations of other methods. Therefore, the application of the elliptical function provides a generalized approach that incorporates other methods as special cases (e.g., zero and infinite focal distances).

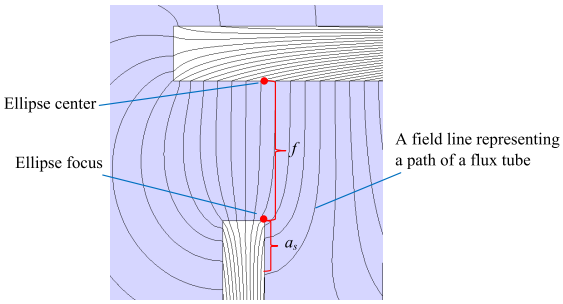


**FIGURE 8.** Approximation of a flux tube path with a 1/4 elliptical arc in the side air gap $R_{g2}$ region shown in Fig. 7.

#### 1) CALCULATION OF THE RELUCTANCES USING A 1/4 ELLIPTICAL ARC FUNCTION

In this study, two types of stray path are considered: elliptical arcs that represent either a quarter (1/4 ) or half (1/2 ) of the circumference of a complete ellipse. For 1/4 elliptical arc paths, the foci of the associated imaginary ellipse are located on different sides of an air gap between the core regions, as illustrated in Fig. 8. It should be mentioned that, whereas 3D FEA modeling is used to verify both the ND-MEC and NT-PEM proposed in this study, figures illustrating the 2D magnetic field distribution are used for discussion purposes due to the clarity of the magnetic field lines. For 1/4 elliptical

arc paths, the total air gap length is half the focal distance, and the parameter $a_s$ determines the distance between the air gap and the center of the associated flux tube. Therefore, by defining the maximum value of $a_s$ and the increment $a_{s1}$, the number of parallel flux tubes for the same effective area can be defined. Each of these contributes to the total reluctance of a particular stray flux path as

$$R_{eq.s} = \left(\sum_k \frac{1}{R_s(a_{s(k)})}\right)^{-1} = \left(\sum_k \frac{\mu_0 A_s(a_{s1})}{l_s(a_{s(k)})}\right)^{-1} \quad (9)$$

$$a_{s(k+1)} = 2a_{s1} + a_{s(k)} \quad (10)$$

where $R_s$ is the reluctance of a single flux tube (1/H), $l_s$ is the length of the associated path (m), and $A_s$ is the cross-sectional area associated with the path ($m^2$). Ideally, the flux tubes cover all of the available area and occupy all of the free space. However, the effect of adding new flux tubes diminishes as their number increases due to the gradual increase in their length. Therefore, it is reasonable to limit $a_s$ based on the geometry of a particular stray region. For 1/4 elliptical arc path lengths, $l_s$ is calculated as

$$l_{s(1/4)}(a_s) = \frac{1}{4}C(a, e) \quad (11)$$

$$C(a, e) = 4aE(e) \quad (12)$$

$$E(e) = \int_0^{\pi/2} \sqrt{1 - e^2 sin^2\theta}\, d\theta \quad (13)$$

$$a = f + a_s \quad (14)$$

$$e = \frac{f}{a} = \frac{f}{f + a_s} \quad (15)$$

where $C(a, e)$ is the circumference of an ellipse (m), $f$ is the distance between the ellipse center and its focus (m), $a$ is the length of the semi-major axis (m), $e$ is the eccentricity, and $E(e)$ is a complete elliptical integral of the second kind [43]–[45]. Because (13) in general has no analytical solution, an approximation derived by Ramanujan is used [46]:

$$C(ae) \approx \pi \left[3(a + b) - \sqrt{(3a + b)(a + 3b)}\right] \quad (16)$$

$$b = a\sqrt{1 - e} \quad (17)$$

where $b$ is the length of semi-minor axis (m). The proposed approach is used to calculate the following reluctances: $R_{ms}$, $R_{c2s}$, $R_{c1s}$, $R_{g2s}$, $R_{g2so}$, and $R_{g2sb}$ (see Fig. 3 (b)). Although (9)–(17) comprehensively summarize the general form of the proposed approach, specific reluctances and their roles should be discussed in detail. First, $R_{ms}$ is the magnet flux leakage reluctance, which accounts for the flux circulating around the magnet and is not linked with the coil. $R_{ms}$is calculated as

$$R_{ms} = \left(\sum_{a_s} \frac{2\pi a_{s1} r_m \mu_0}{\frac{1}{4}C\left(h_m, \frac{h_m}{h_m + a_s}\right)}\right)^{-1} \quad (18)$$

where $r_m$ is the radius of the magnet (m), and $h_m$ is the magnet height (m). In a similar manner, the path lengths of the other reluctances are calculated using the above expression for the circumference $C$ by (16). This type of leakage is typical for electrical machines [47]. It should be noted that $a_{s1}$ must be sufficiently small in order to approximate the 3D field distribution correctly. Another assumption should be made about the number of steps in (18). For the air region surrounding the magnet, $a_s$ determines the extent to which the core regions contribute to $R_{ms}$ rather than the stray reluctance $R_{c2s}$. In this study, it is assumed that the total area contributing to $R_{ms}$ is smaller than that contributing to $R_{c2s}$. This is based on observations made during FEM analysis. Therefore, the maximum value of $a_s$ in (18) is relatively small. $R_{c2s}$ is the coil to armature stray reluctance, which is calculated as

$$R_{c2s} = \left(\sum_{a_s} \frac{2.35 \cdot 2\pi a_{s1} r_2 \mu_0}{\frac{1}{4}C\left(\frac{3}{2}h_m + a_s, \frac{3h_m}{3h_m + 2a_s}\right)}\right)^{-1} \quad (19)$$

where $r_2$ is the radius of the central section of the armature core (m). $R_{c2s}$ has a very high influence on the overall behavior of the circuit. This is related to the fact that it represents a region surrounding another poorly conducting region (i.e., that of the magnet). Because the magnet permeability is close to the air permeability, a considerable portion of the magnetic flux tends to flow outside the main path through neighboring air regions. It will be shown that the flux through $R_{c2s}$ and the energy stored in this reluctance both are relatively large. The coil to stator stray reluctance $R_{c1s}$ is calculated as

$$R_{c1s} = \left(\sum_{a_s} \frac{3\pi a_{s1} r_2 \mu_0}{\frac{1}{4}C\left(2h_1 + l_{g1} + a_s, \frac{2h_1 + l_{g1}}{2h_1 + l_{g1} + a_s}\right)}\right)^{-1} \quad (20)$$

where $h_1$ is the height of the pole at the center of the stator (m), and $l_{g1}$ is the length of the main gap (m). Similar to the previously discussed reluctance $R_{c2s}$, this reluctance accounts for the part of the main flux arriving directly at the bottom plate of the stator, avoiding the main gap. However, this reluctance is rather large because the paths that the fluxes take are much longer. Moreover, the pole at the center of the stator makes the main path much more conductive in this section of the MC, in contrast with the upper section.

Finally, there are three stray reluctances and one leakage reluctance associated with the side gap $R_{g2}$. The path lengths for all three stray reluctances are described by 1/4 elliptical arc functions. The first reluctance, $R_{g2s}$, accounts for the flux passing from the stator to the armature upper plate via internal paths and is described by

$$R_{g2s} = \left(\sum_{a_s} \frac{3a_{s1} l_5 \mu_0}{\frac{1}{4}C\left(l_{g2} + a_s, \frac{l_{g2}}{l_{g2} + a_s}\right)}\right)^{-1} \quad (21)$$

where $l_5$ is the length of the core in the $z$-direction (m), and $l_{g2}$ is the length of the side gap determining the main flux path (m). $R_{g2s}$ reluctance plays a considerable role because the main flux path reluctance of the side air region $R_{g2}$ is rather large, and it is surrounded by other air regions. Consequently, the permeances of the adjacent paths are comparable with the permeance of the main path. This can be seen clearly for large air gaps. Because the main path is narrow,

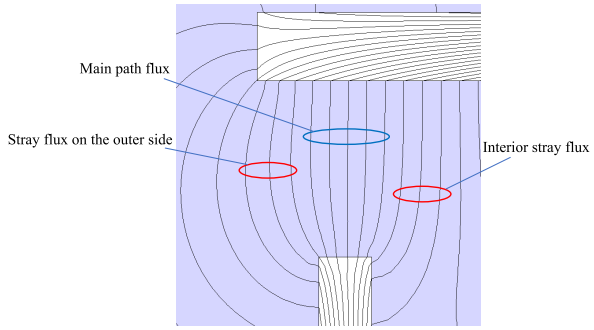


**FIGURE 9.** Stray fluxes in the vicinity of the side air gap region shown in Fig. 7.

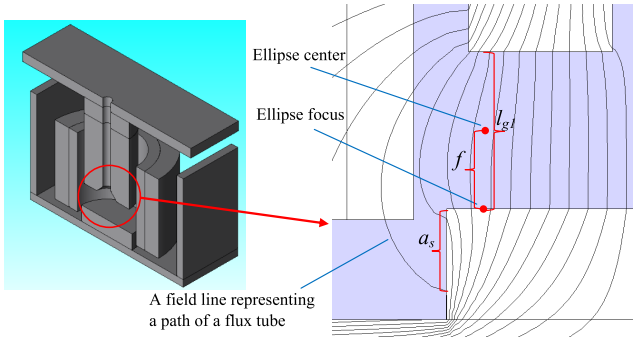


**FIGURE 10.** Approximation of a flux tube path with a 1/2 elliptical arc in the main air gap $R_{g1}$ region.

a proportion of the flux deviates from the main flux path to the interior region shown on the right side of Fig. 9. Identical reasoning can be applied to account for the fluxes deviating to exterior regions shown on the left side of Fig. 9, which are represented by the reluctance

$$R_{g2so} = \left(\sum_{a_s} \frac{2a_{s1}l_5\mu_0}{\frac{1}{4}C(l_{g2}+a_s, \frac{l_{g2}}{l_{g2}+a_s})}\right)^{-1} \tag{22}$$

However, this reluctance does not have as much influence on the magnetic field distribution because $a_s$is limited by the length of the extended core section on the left side of the air gap in Fig. 9, which is relatively short. Therefore, the effective area of the stray flux region is relatively small. Finally, part of the flux flows from the top of the stator wall to the sides of the armature upper plate. This is taken into account by the following reluctance

$$R_{g2sb} = \left(\sum_{a_s} \frac{\frac{1}{2}a_4(a_{s1}+\frac{l_3-l_5}{2})\mu_0}{\frac{1}{4}C(l_{g2}+a_s, \frac{l_{g2}}{l_{g2}+a_s})}\right)^{-1} \tag{23}$$

where $l_3$ is the z-direction length of the stator (m)

It should be mentioned that the accurate calculation of the effective areas of the stray path flux tubes is another challenge, for which a reliable methodology has not yet been developed. Moreover, a flux tube cross-section can vary along the length of the tube depending on the shape and size of adjacent core sections. Therefore, certain assumptions have been made for every reluctance when approximating $A_s$ in (9). For most reluctances, the effective cross-sectional areas are assumed to be 3/2 the area at the beginning of the corresponding flux tube. However, several reluctances require additional modification. Specifically, a multiplier of 2 is used in (18), and one of 2.35 is used in (19). This can be interpreted as an increase in the flux tube cross-sectional area towards one side due to the larger available area (e.g., the plates on the top and bottom sections of the contactor).

#### 2) CALCULATION OF THE RELUCTANCES USING A 1/2 ELLIPTICAL ARC FUNCTION

For 1/2 elliptical arcs, it is assumed that the center of the ellipse is at the center of the air gap and the core regions are at the focal distance, as illustrated in Fig. 10 for the main gap region. Therefore, the focal distance $f$ is half the air gap length, and path length $l_s$ is half the ellipse circumference:

$$l_{s(1/2)}(a_s) = \frac{1}{2}C(a, e) \tag{24}$$

The rest of the argument is the same as for the 1/4 elliptical arc paths, and (14)–(17) are used to calculate the circumference by (24). Only two reluctances in the ND-MEC use this expression. The first is the main air gap stray reluctance:

$$R_{g1s} = \left(\sum_{a_s} \frac{3\pi a_{s1}r_1\mu_0}{\frac{1}{2}C(\frac{1}{2}l_{g1}+a_s, l_{g1}/(l_{g1}+2a_s))}\right)^{-1} \tag{25}$$

Fluxes that avoid the main gap are usually addressed using traditional MEC methods in the same manner as leakage fluxes because they do not contribute energy to the main air gap. However, this study makes a distinction between stray and leakage fluxes because the former still contribute to the contactor output force. The flux for the reluctance $R_{g1s}$ still connects the stator with the armature, partially contributing to the total linked flux. The consequences of this observation are discussed in more detail in Section VI. Finally, the side gap flux leakage reluctance is expressed in the following way:

$$R_{g2se} = \left(\sum_{a_s} \frac{2a_{s1}l_5\mu_0}{\frac{1}{2}C(f_{g2f}+a_s, \frac{f_{g2f}}{f_{g2f}+a_s})}\right)^{-1} \tag{26}$$

where $a_5$ and $a_3$ are the lengths of the upper plate of the armature and the bottom plate of the stator (m), respectively. Reluctances (22), (23), and (26) are all connected in parallel and are represented by a single reluctance in Fig. 3 (b) calculated as

$$R_{g2f} = \left(\frac{1}{R_{g2so}} + \frac{1}{R_{g2sb}} + \frac{1}{R_{g2se}}\right) \tag{27}$$

### D. VERIFICATION OF THE ELLIPTICAL FUNCTION FOR STRAY PATH RELUCTANCE CALCULATION

In order to verify the validity of the proposed method for stray path evaluation, an analysis of the simple magnetic circuit shown in Fig. 11 (a) is conducted. This model consists of one coil and one air gap located so that the field distribution

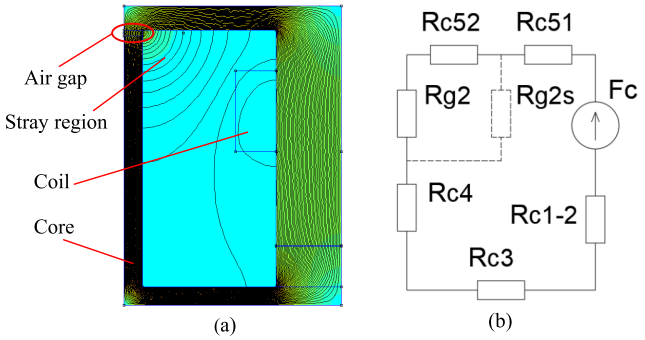


**FIGURE 11.** A simplified side air gap circuit model for the verification of the proposed elliptical function. (a) FE and (b) the MEC and ND-MEC models.

**TABLE 2.** Magnetic flux density in the FEA and MEC/ND-MEC solutions for the simplified model in Fig. 11. Rows highlighted with a ∗ notation show that an MEC without stray reluctance $R_{g2s}$ cannot model the complete field distribution.

| Calculation method | Air gap flux density $B_{g2}$, T | Core flux density $B_{c1\text{-}2}$, T |
|---|---|---|
| FEM, no interior air | 1.75 | 0.51 |
| MEC, no $R_{g2s}$ | 1.77 | 0.51* |
| FEM, including interior air | 1.75 | 0.91* |
| ND-MEC, including $R_{g2s}$ | 1.77 | 0.92* |

* Highlighted values with * notation must agree for the validity of the MEC or ND-MEC model

is similar to that in the interior region of the side air gap of the original contactor shown in Figs. 8 and 9. The equivalent magnetic circuit shown in Fig. 11 (b) consists of several core regions with high permeability, one low-permeability air gap region, $R_{g2}$, and the stray flux reluctance $R_{g2s}$ which is the main focus of this experiment. Linear material properties are used in this experiment to prevent core saturation from interfering with the results. Two experiments are conducted in FEA. First, the interior air region is excluded from the finite element (FE) model, implying that no stray fluxes are allowed in FEA. Following this, the interior air region is included in the FE model to model interior stray fluxes. As a comparison, for the MEC in Fig. 11 (b) circuit equations are also solved for the two cases. First, $R_{g2s}= 0$, corresponding to a traditional MEC approach. Second, $R_{g2s}$ is calculated using the elliptical function discussed in Section III, using the step value $a_{s1}= 0.1$ mm, corresponding to the ND-MEC method. Table 2 shows that the FEA and MEC solutions match exactly when interior air is excluded. It should be noted that the circuit with $R_{g2s}= 0$ corresponds to the main flux path MEC. When interior air is included, the air gap flux density in the FE solution remains the same, but core flux density almost doubles. This means that the total flux doubles as well; however, this extra flux does not pass through the main gap. Consequently, this is not reflected in the MEC when $R_{g2s}= 0$. When $R_{g2s}$ is included in the MEC, as in the proposed ND-MEC method that uses the proposed elliptical function, the results match those of the FEA with an error of only 1%.

It should be mentioned that, when stray fluxes are allowed only near the gap and $a_s$ is small, the influence of $R_{g2s}$ diminishes and the error approaches 50%. In contrast, the error falls to 1% when all of the internal areas contribute to the stray flux. This simple experiment illustrates that the proposed elliptical function and stray flux in the ND-MEC can model stray field effects with high accuracy.

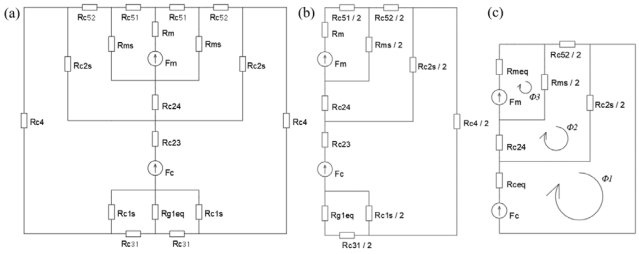


**FIGURE 12.** Simplification of the ND-MEC of the MC in Fig. 3 (b) after (a) series and parallel reluctances are combined and (b) symmetry in the circuit is used. (c) Final version of the simplified circuit.

## IV. FORMULATION OF EQUIVALENT CIRCUIT EQUATIONS AND SOLUTION FOR THE ND-MEC

Fig. 3 (b) represents the proposed ND-MEC in its most comprehensive form, but it can be simplified if the series and parallel reluctances are combined and the symmetry of the circuit is considered. First, reluctances that are clearly in series or parallel are used to calculate equivalent reluctances, resulting in the circuit shown in Fig. 12 (a). The reluctances in Fig. 12 (a) can be calculated using

$$R_{g1eq} = R_{c11} + R_{c22} + \left(\frac{1}{R_{g1s}} + \frac{1}{R_{g1} + R_{c12} + R_{c21}}\right)^{-1} \quad (28)$$

$$R_{g2eq} = R_{c42} + R_{c53} + \left(\frac{1}{R_{g2}} + \frac{1}{R_{g2f}}\right)^{-1} \quad (29)$$

$$R_{c4} = R_{c32} + R_{c41} + \left(\frac{1}{R_{g2eq}} + \frac{1}{R_{g2s}}\right)^{-1} \quad (30)$$

Furthermore, because the structure of the circuit on the left and right sides of the central branch *R1-R2-R5* is identical, the ND-MEC can be reduced to the state shown in Fig. 12(b). Finally, the reluctances in Fig. 12 (c) are calculated as a combination of previous reluctances:

$$R_{ceq} = R_{c23} + \frac{1}{2}R_{c4} + \left(\frac{2}{R_{c1s}} + \frac{1}{R_{g1eq} + \frac{1}{2}R_{c31}}\right)^{-1} \quad (31)$$

$$R_{meq} = R_m + \frac{1}{2}R_{c51} \quad (32)$$

The final version of the circuit, shown in Fig. 12 (c), is solved using the mesh current method. When the loop fluxes $\Phi_1$–$\Phi_3$ are obtained, the fluxes in the ND-MEC branches of interest are calculated using the known rules of the mesh current method. In the formulation of the final system of equations in matrix form (33), $\Phi_1$ is the flux of the loop with the coil mmf source $F_c$, $\Phi_2$ is the flux of the

loop between the circuit and magnet loops, and $\Phi_3$ is the flux of the loop with the magnet mmf source $F_m$ (Wb), as shown in Fig. 12 (c).

$$\begin{bmatrix} F_c \\ 0 \\ F_m \end{bmatrix} = \begin{bmatrix} R_{11} & -\frac{R_{c2s}}{2} & 0 \\ -\frac{R_{c2s}}{2} & R_{22} & -\frac{R_{ms}}{2} \\ 0 & -\frac{R_{ms}}{2} & R_{33} \end{bmatrix} \cdot \begin{bmatrix} \Phi_1 \\ \Phi_2 \\ \Phi_3 \end{bmatrix} \quad (33)$$

$$R_{11} = R_{ceq} + \frac{R_{c2s}}{2} \quad (34)$$

$$R_{22} = R_{c24} + \frac{R_{c2s} + R_{ms} + R_{c52}}{2} \quad (35)$$

$$R_{33} = R_{meq} + \frac{R_{ms}}{2} \quad (36)$$

Steady-state experiments are conducted for the closed and open states of the contactor and compared to the 3D FEA results shown in Fig. 13 in order to verify the ability of the ND-MEC to model the magnetic field distribution. In these two experiments, the armature position is kept constant, and changes in the main air gap flux density due to variation in the current are monitored. The main air gaps in the open and closed states are 0.1 mm and 7.1 mm, respectively, leading to the saturation of the core in the closed state. This is reflected in the shape of the flux density curve in Fig. 13 (a). In contrast, the main flux is much lower in the open state, resulting in a lower flux density and the nearly linear relationship between flux density and current. The maximum difference between the ND-MEC and 3D FEM solutions is about 6%.

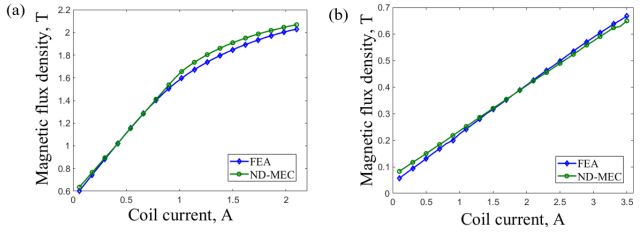


**FIGURE 13.** Change in the main air gap magnetic flux density with coil current in the (a) closed and (b) open states of the MC.

Additionally, the flux distribution in different branches of the ND-MEC is assessed for the maximum current used in the analysis shown in Fig. 13. It is notable that most of the total flux, which is flux $\Phi_{c23}$ in reluctance $R_{c23}$, passes through the main gap in the closed state, as shown in Table 3. This is expected because the air gap is small, and the main gap stray flux is extremely low. However, the stray fluxes in the upper section of the armature ($\Phi_{g2s}\Phi_{g2f}$, and $\Phi_{c2s}$) are already considerable. It can be observed that about half of the main flux flows along the main path (flux $\Phi_m$ through reluctance $R_m$), whereas as much as one-third of the total flux follows the stray route $R_{c2s}$. The side gap flux distribution is also affected by stray paths, with $\Phi_{g2s}$ almost twice as high as the side gap flux $\Phi_{g2}$ in $R_{g2}$. This illustrates the importance of stray flux modeling in this contactor. This argument is

**TABLE 3.** Flux distribution in the branches of the ND-MEC in its open and closed states.

| Reluctance | Flux in closed state, Wb·10$^{-5}$ | Flux in open state, Wb·10$^{-5}$ |
|---|---|---|
| Main gap *Rg1* | 35.2 | 12.8 |
| Side gap *Rg2** | 7.4 | 2.7 |
| Stator pole *Rc11* | 36.5 | 23.8 |
| Armature pole, coil *Rc23* | 39 | 32.5 |
| Stator plate *Rc31** | 36.1 | 11.9 |
| Stator wall *Rc42** | 13.1 | 8.7 |
| Armature plate *Rc52** | 11.5 | 10.2 |
| Magnet *Rm* | 20.8 | 18.8 |
| Main gap stray path *Rg1s** | 1.3 | 11 |
| Side gap stray path *Rg2s** | 6.3 | 7.6 |
| Side gap stray path *Rg2f** | 5.7 | 6 |
| Magnet leakage *Rms** | 1.1 | 0.8 |
| Coil to stator stray path *Rc1s** | 1.2 | 4.3 |
| Coil to armature stray path *Rc2s** | 8 | 6 |

* Fluxes in symmetric branches of the ND-MEC are listed as the sum of the branch fluxes

also supported by the analysis of the flux distribution in the open state of the contactor. The main gap stray flux $\Phi_{g1s}$ flowing through reluctance $R_{g1s}$ is almost as high as the main flux $\Phi_{g1}$. This is because the main gap is larger in an open state, and the difference in reluctance between the stray and main flux paths falls. It should be noted that, because stray path lengths are longer, stray reluctances store more energy than main path reluctances, as will be shown in Section VI. These results illustrate the technical superiority of the proposed ND-MEC over traditional MECs because it can be used to gain valuable information about the flux distribution, which has a significant effect on the overall performance of the MC.

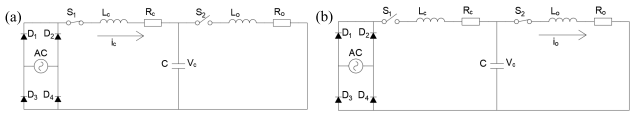


**FIGURE 14.** Electrical circuit of the MC for the (a) closing and (b) opening operations.

## V. FORMULATION OF COUPLED ELECTRIC-MAGNETIC-MECHANICAL EQUATIONS FOR THE ANALYSIS OF MC DYNAMICS

### A. AFORMULATION OF THE ELECTRICAL CIRCUIT EQUATIONS FOR THE MC

The electrical circuit for a contactor includes a voltage source, a capacitor, and closing and opening coils as shown in Fig. 14. When switch *S1* is closed and switch *S2* is open, the contactor's closing coil is connected to the voltage source, which simultaneously charges a capacitor [24]:

$$V_s = iR_c + L_c\frac{\partial i}{\partial t} + V_c \quad (37)$$

where $R_c$ is the closing coil resistance (ohm), $L_c$ is the closing coil inductance (H), and $V_c$ is the capacitor voltage (V). However, because back electromotive force (emf) can be

induced by both changes in the current and changes in armature position, (37) is written as

$$V_s = iR_c + L_{ci}\frac{\partial i}{\partial t} + L_{cx}\frac{\partial x}{\partial t} + V_c \tag{38}$$

$$L_{ci} = \frac{d\lambda_c(i,x)}{di} \tag{39}$$

$$L_{cx} = \frac{d\lambda_c(i,x)}{dx} \tag{40}$$

$$V_c = \frac{1}{C}\int idt \tag{41}$$

where $L_{ci}$ is the change in flux linkage due to the change in current $di$ (H), $L_{cx}$ is the change in flux linkage due to displacement $dx$ (Wb/m), and $C$ is the capacitance (F).

On the other hand, when switch *S1* is closed and switch *S2* is open, the capacitor that was charged during the closing of the MC energizes the opening coil. This produces a repulsive force between the coil and the magnet, moving the armature away from the stator. Equations (42)–(45) summarize the circuit equations for the opening operation

$$V_c = iR_o + L_{oi}\frac{\partial i}{\partial t} + L_{ox}\frac{\partial x}{\partial t} \tag{42}$$

$$L_{oi} = \frac{d\lambda_o(i,x)}{di} \tag{43}$$

$$L_{ox} = \frac{d\lambda_o(i,x)}{dx} \tag{44}$$

$$V_c = V_0 - \frac{1}{C}\int idt \tag{45}$$

where $R_c$, $L_{oi}$, and $L_{ox}$ are opening coil parameters that are identical to $R_c$, $L_{ci}$, and $L_{cx}$, respectively.

### B. FORMULATION OF MOTION EQUATIONS

The motion of the armature is described by Newton's equation of motion neglecting friction:

$$m\frac{d^2\vec{x}}{dt^2} = \vec{F}_{grav} + \vec{F}_{mag} + \vec{F}_{spring} \tag{46}$$

where $m$ is the mass of the armature with a moving contact (kg), $F_{grav}$ and $F_{mag}$,are the gravitational and magnetic forces, respectively, acting on the armature (N), and $F_{spring}$ is the elastic force of the opening spring (N). The velocity and displacement of the armature are calculated as

$$v = \int \frac{F_{grav} + F_{mag} + F_{spring}}{m}dt \tag{47}$$

$$x = \int\left(\int \frac{F_{grav} + F_{mag} + F_{spring}}{m}dt\right)dt \tag{48}$$

### C. FORMULATION OF THE TIME DIFFERENCE METHOD FOR THE MC

The above equations describe the complete dynamics of the contactor, but solving them analytically is generally not possible unless additional techniques are employed. In this study, the TDM is implemented to convert the differential equations (38)–(48) to their algebraic form [48]–[50]. As a result, *B–H* material non-linearities and the complicated association between the stray flux reluctances and displacement can be evaluated at every time step, which further contributes to the accuracy of the force calculation discussed in Section VI. For the $n^{th}$ time step of length $dt$, the governing dynamics equations for the closing operation are derived based on (38)–(41) as

$$V_s^n = \left(i^{n-1} + di^n\right)R_c + L_{ci}^{n-1}\frac{di^n}{dt} + L_{cx}^{n-1}\frac{dx^n}{dt} \tag{49}$$

$$L_{ci}^n = \frac{\lambda_c^n(i,x) - \lambda_c^{n-1}(i,x)}{di^n} \tag{50}$$

$$L_{cx}^n = \frac{\lambda_c^n(i,x) - \lambda_c^{n-1}(i,x)}{dx^n} \tag{51}$$

$$V_c^n = V_c^{n-1} - \frac{1}{C}\left(i^{n-1} + di^n\right) \tag{52}$$

Similarly, for the opening operation (42)–(45) are written as

$$V_c^n = \left(i^{n-1} + di^n\right)R_o + L_{oi}^{n-1}\frac{di^n}{dt} + L_{ox}^{n-1}\frac{dx^n}{dt} \tag{53}$$

$$L_{oi}^n = \frac{\lambda_o^n(i,x) - \lambda_o^{n-1}(i,x)}{di^n} \tag{54}$$

$$L_{ox}^n = \frac{\lambda_o^n(i,x) - \lambda_o^{n-1}(i,x)}{dx^n} \tag{55}$$

$$V_c^n = V_c^{n-1} - \frac{1}{C}\left(i^{n-1} + di^n\right)dt \tag{56}$$

The above equations can be rearranged to calculate the change in the current $di$ for the closing (57) and opening (58) regimes:

$$di^n = \frac{-\frac{1}{C}i^{n-1}(dt)^2 + \left(V_s^n - V_c^{n-1} - i^{n-1}R_c\right)dt - L_{cx}^{n-1}dx^n}{\frac{1}{C}(dt)^2 + R_c dt + L_{ci}^{n-1}} \tag{57}$$

$$di^n = \frac{-\frac{1}{C}i^{n-1}(dt)^2 + \left(V_c^{n-1} - i^{n-1}R_o\right)dt - L_{ox}^{n-1}dx^n}{\frac{1}{C}(dt)^2 + R_o dt + L_{oi}^{n-1}} \tag{58}$$

The change in the current $di$ for the first time step $n$ =1 needs to be calculated differently because the $(n\text{-}1)^{th}$ time step does not exist. Therefore, the initial change in the closing current $di^1$is calculated as

$$di^1 = \frac{V_s^1 dt}{\frac{1}{C}(dt)^2 + R_c dt + L_{ci}^0} \tag{59}$$

where $L_{ci}^0$ is the initial value of the closing coil inductance (H). Similarly, the initial change of the opening current is calculated as

$$di^1 = \frac{V_c^1 dt}{\frac{1}{C}(dt)^2 + R_o dt + L_{oi}^0} \tag{60}$$

where $L_{oi}^0$ is initial opening coil inductance (H). These inductances can be calculated based on ND-MEC parameters

using (67), as shown at the bottom of this page. Finally, the motion of the armature is determined using (61)–(63).

$$m\frac{d^2x^n}{dt^2} = F_{grav} + F^n_{mag} + F^n_{spring} = F^n_{net} \tag{61}$$

$$v^n = v^{n-1} + \left(\frac{F^n_{net}}{m}\right)dt \tag{62}$$

$$dx^n = v^{n-1}dt + \frac{1}{2}\left(\frac{F^n_{net}}{m}\right)(dt)^2 \tag{63}$$

By analyzing (49)–(63), it can be concluded that the above equations describe the closely intertwined electrical-magnetic-mechanical behavior of the MC. For instance, (49) and (53) describe the electrical state of the opening and closing coils, which is influenced by the inductances (50), (51), (54), and (55), which depend on the change in the linked magnetic flux, which depends on the change in the reluctances of the MEC, which in turn depends on the change in the position of the armature. Therefore, standard methods that rely only on decoupled problem analysis will provide flawed results when the complete dynamic behavior of the MC is analyzed. As a result, the application of the complete proposed method is essential for an accurate representation of MC dynamics.

## VI. FORMULATION OF THE PROPOSED NT-PEM

Traditionally, MEC methods are applied only to quasi-static or periodic problems which arise due to constant or harmonic excitation. However, even for harmonic excitation, the response of a system can be non-linear due to non-linearities in the ND-MEC parameters. Therefore, it is essential that the non-linear behavior of the circuit parameters and its effects on the output performance of a machine are accurately taken into account, and this is addressed by the proposed ND-MEC. However, analyzing the complete dynamics of electrical machines using MEC methods is subject to complications because dynamics-defining parameters such as force and inductance depend on the time derivatives of other parameters.

Calculating these parameters using the proposed NT-PEM method is discussed in this Son. However, it should be stressed that the results of force and inductance calculation depend not only on the input data for the current time step but also on the data from the previous step. Therefore, a combination of the ND-MEC, the TDM, and the path energy method for the calculation of electromagnetic force naturally extends the use of the equivalent circuit method to non-linear analysis in the time domain.

### A. CALCULATION OF THE OUTPUT FORCE OF THE MC

#### 1) FORCE CALCULATION METHOD BASED ON THE INDUCTANCE CHANGE

In general, electromagnetic force can be calculated as

$$F_{mag} = -\left.\frac{\partial W^*_{mag}}{\partial x}\right|_{i=const} \tag{64}$$

where $W*_{mag}$ is the co-energy (J). This can be further expanded as

$$W^*_{mag} = \frac{1}{2}i\lambda = \frac{1}{2}Li^2 \tag{65}$$

$$F_{mag} = -\frac{1}{2}i^2\frac{\partial L(x)}{\partial x} \tag{66}$$

where $i$ is the current (A), $\lambda$ is the flux linkage (Wb), and $L$ is the coil inductance (H). This approach is commonly used for calculating electromagnetic forces in actuators [51]–[55]. However, in combination with the ND-MEC, $L(x)$ in (66), as shown at the bottom of this page can be expressed analytically using the parameters of the equivalent circuit as

$$L(x) = \frac{\lambda(x)}{i} = N^2\Lambda_{tot}(x) = \frac{N^2}{R_{tot}(x)} \tag{67}$$

where $\Lambda_{tot}$ is the total permeance of the magnetic circuit with respect to the coil mmf source (H), and $R_{tot}$ is the total reluctance (1/H). $R_{tot}(x)$ is calculated by (68). As previously discussed in Section III, most air reluctances are a function of the armature position and, hence, of the displacement $x$. Therefore, it is possible to obtain an analytical expression for $\partial L(x)/\partial x$ in (66) by substituting (68) into (67), and differentiating the latter. In this way, $\partial L(x)/\partial x$ can be represented by a polynomial function of position $x$. For the studied circuit, (69) is obtained

Therefore, electromagnetic force (66) becomes a function of the current armature position $x$ rather than the change in its position $dx$. This avoids certain numerical difficulties when employing TDM. Equation (69) illustrates a useful feature of the ND-MEC method that allows it to account for variations in stray and leakage reluctances in a magnetic circuit, clearly expressing them as functions of MC displacement. Obtaining a single equation for the derivative of the inductance can be extremely useful for the convenient analysis of force or torque

$$R_{tot}(x) = R_{ceq}(x) + \left[\left(\left(\frac{1}{R_{meq}} + \frac{2}{R_{ms}}\right)^{-1} + \frac{1}{2}R_{c52} + R_{c24}\right)^{-1} + \frac{2}{R_{c2s}(x)}\right]^{-1} \tag{68}$$

$$\frac{\partial L(x)}{\partial x} = \frac{-1.5\cdot10^{-9}}{x^2+0.92\cdot x+0.21} - \frac{2.3\cdot10^{-10}}{x^2+x\cdot7.2\cdot10^{-3}+1.3\cdot10^{-5}} - \frac{6.2\cdot10^{-13}}{x^2+x\cdot1.95\cdot10^{-3}+9.5\cdot10^{-7}} - \frac{7.6\cdot10^{-11}}{x^2+x\cdot5.33\cdot10^{-3}+7.1\cdot10^{-6}} - \frac{1.1\cdot10^{-10}}{x^2+x\cdot5.7\cdot10^{-4}+8.2\cdot10^{-8}} - \frac{2.9\cdot10^{-10}}{x^2+0.01\cdot x+3.9\cdot10^{-5}} \tag{69}$$

in a variety of electrical machines in which the electromagnetic force is reactive in nature.

However, a complication arises due to both the magnet and coils being present in this contactor design. It can be observed that the influence of the magnet is not included in (66). Therefore, the holding force of the magnet in a closed state cannot be calculated. Calculating the repulsive force between the opening coil and the magnet is also essential for the analysis of the opening process. This is a significant drawback of utilizing the change in inductance, thus limiting its applicability in the accurate calculation of force in PM-type MCs. In order to address these problems, a path energy method is proposed in the following subsection.

### 2) THE PROPOSED FORCE CALCULATION METHOD BASED ON CHANGE IN PATH ENERGY

In this sub-section, force calculation based on the change in path energy is conducted, addressing the problem stated in the previous sub-section. Energy methods are generally much more fundamental in nature and account for multiple energy contributions [56]. Because this approach uses the change in energy, to which both coils and magnet contribute, it accounts for any variation in the parameters, such as current amplitude or change in sign, magnet demagnetization, or the variation in distance between the coils and the magnet [57], [58]. The electromagnetic force is calculated as

$$F_{mag} = -\frac{\partial W_{mag}}{\partial x}\bigg|_{i=const} \tag{70}$$

$$W_{mag} = \sum_i V_i \int_0^{H_i} B_i dH \tag{71}$$

where $V_i$ is the volume of the regions with constant flux densities $B_i$ and field intensities $H_i$ ($m^3$). Energy is summed for all non-leakage air reluctances. However, different air reluctances contribute differently to the generation of force because the magnetic flux direction does not necessarily coincide with the motion direction. Commonly, when the main magnetic path circuit in Fig. 2 is analyzed, only the main and side gap reluctances and their energies are considered. This is because the main magnetic flux is exactly normal to the core poles, and its direction always coincides with the direction of the displacement vector. However, magnetic fluxes in the other air reluctances of the complete ND-MEC in Fig. 3 (b) also contribute to force because they are not necessarily perpendicular to the direction of motion. Therefore, a novel approach for estimating these contributions is proposed. In order to account for variations in energy contributions depending on the air paths the magnetic fluxes take, (71) is written as

$$W_{mag} = \sum_i k_{wi} \frac{B_i H_i}{2} \cdot A_i l_i \tag{72}$$

$$k_{wi(1/4)} = \left(\frac{f_i + a_{s\cdot avi}}{l_{si}(a_{s\cdot avi})}\right)^2 \tag{73}$$

$$k_{wi(1/2)} = \left(\frac{2\,(f_i + a_{s\cdot avi})}{l_{si}(a_{s\cdot avi})}\right)^2 \tag{74}$$

where $k_{wi}$ is a coefficient that identifies the fraction of the $i$-air path energy participating in force production, and $a_{s.avi}$ is the average value of the parameter $a_s$, (m). The subscripts 1/4 and 1/2 in (73) and (74) refer to quarter- and half-ellipse circumference paths, respectively. The geometrical meaning of $k_w$ is the ratio of semi-major axis $a$, which is proportional to the normal component of flux density vector $B_n$, to the length of the elliptical path, which is proportional to the amplitude of the total vector $B$. This approach is only approximate because the actual value of $B_n$ changes along the length of the elliptical arc. However, it must be noted that this approach allows $k_w$ to be calculated for every time step, meaning that the effects of any change in position or current are reflected in (72). This method is in good agreement with FEA results, as shown in the next Section.

**TABLE 4. Energy stored in the air reluctances at the end of opening operation of the MC and the corresponding values of the correction coefficient, $k_w$.**

| Reluctance | Energy, J·10$^{-3}$ | $k_w$ |
|---|---|---|
| Main gap *Rg1* | 9.4 | 1 |
| Side gap *Rg2** | 2.3 | 1 |
| Main gap stray *Rg1s** | 8.8 | 0.62 |
| Side gap stray *Rg2s** | 6.9 | 0.63 |
| Side gap stray *Rg2f** | 7.2 | 0.75 |
| Upper coil stray *Rc2s** | 33.1 | 0.58 |
| Bottom coil stray *Rc1s** | 6.6 | 0.77 |

* Energies of symmetric branches of ND-MEC are listed as the sum of the symmetric branch energies

Table 4 shows that the stored energy varies greatly among the air reluctances in the ND-MEC. This state is chosen because of large main gaps since otherwise the energy stored in the main path air gaps is too small. It can be seen that the energy stored along the path associated with the reluctance $R_{c2s}$ is more than three times higher than the main air gap energy, illustrating the significance of the influence that this region has on the overall behavior of the MC. On the other hand, its actual contribution to the force is almost two times smaller due to the considerable bending of the flux path, as reflected in the value of the associated $k_w$.

By analyzing Table 4, it can be concluded that a model that considers only main flux air path contributions would predict lower output forces. On the other hand, a model that does not correct for path bending or the misalignment between the force and displacement vectors would predict unrealistically large forces. Therefore, it is extremely important to account for contributions of all air paths and apply corrections for the factors that are otherwise ignored in traditional MEC methods. The TDM form of the force calculation equation (70) is given by

$$F^n_{mag} = \frac{W^n_{mag}\,(i,x) - W^{n-1}_{mag}\,(i,x)}{dx^n} \tag{75}$$

where the $n^{th}$ step components are calculated using (72)–(74).

### B. COMBINATION OF THE ND-MEC, TDM, AND PATH ENERGY METHOD INTO THE NT-PEM

The previous sub-section explicitly demonstrates that path energies, including those of stray paths which are the main focus of Sections III and IV, play a significant role in the dynamic behavior of an MC. By substituting (75) into (61), a complete electrical-magnetic-mechanical coupled problem for the dynamics of an MC can be formulated. It is solved with the NT-PEM, which is naturally derived from the combination of the ND-MEC, TDM, and path energy method. As discussed in Section V lumped electrical parameters, such as inductances, represent a simplification of the significantly more complicated magneto-mechanical response of the ND-MEC to applied voltage and mechanical constraints. Therefore, solving the ND-MEC at every time step leads to an accurate representation of the physical behavior of the MC, whereas the application of the TDM allows time-derivative dependent variables such as inductance and electromagnetic force to be calculated. Consequently, output parameters of interest such as displacement, velocity, output force, and electric current are obtained as a function of time, which is essential for understanding the dynamic performance of an MC.

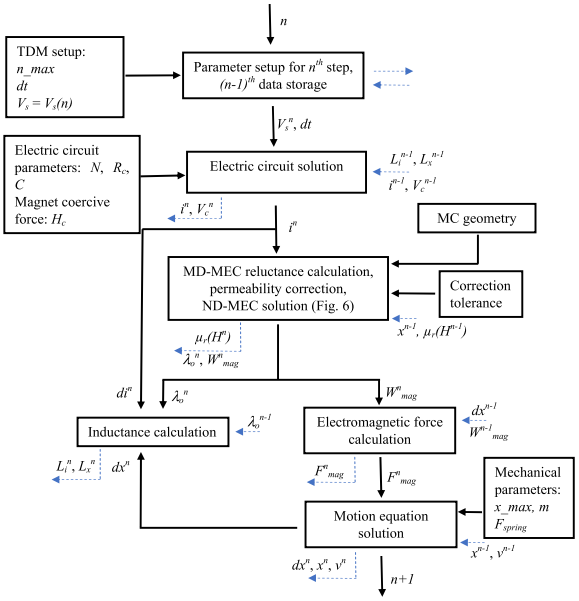


**FIGURE 15.** The proposed algorithm for the $n^{th}$ time step calculation of the proposed NT-PEM combining the ND-MEC with the TDM and the path energy calculation method. Dashed lines indicate the input and output variables for the corresponding subroutines.

Fig. 15 shows that the proposed NT-PEM algorithm, which consists of several sub-routines performing calculations on the current step and an additional sub-routing program that acts as data storage and as an access point for different time steps. The presented algorithm illustrates the calculation procedure for the $n^{th}$ step and is executed repeatedly for all $n_{max}$ steps. Boxes with no input variables in Fig. 15 represent analysis constants such as MC geometry, magnetic and electric circuit parameters, and TDM parameters. The special attributes of the calculation of the first step were discussed previously in Section V. Because almost all calculations conducted on the $n^{th}$ step require $(n\text{-}1)^{th}$ step data as an additional input, associated parameters are illustrated by the dashed inward arrows in Fig. 15. Similarly, all data of interest calculated at the current step is stored in the relevant section of the managing sub-program, and associated parameters are illustrated by the dashed outward arrows.

While any combination of calculated parameters can be used to analyze the results, the parameters of most interest in this study are electrical current, electromagnetic force, and output displacement. These are used to evaluate MC performance and verify the proposed method in the next Section.

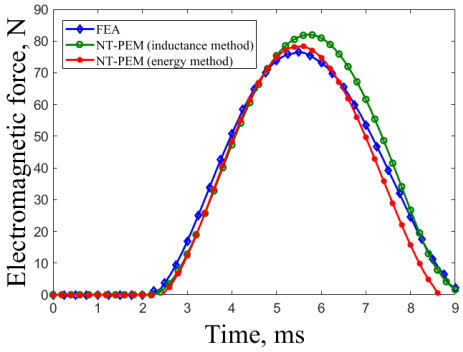


**FIGURE 16.** Electromagnetic force versus time during MC closing operation computed using FEM and the two MEC methods.

## VII. MC PERFORMANCE EVALUATION USING THE NT-PEM AND THE VERIFICATION OF THE PROPOSED METHOD

### A. CLOSING OPERATION OF THE MC

The applicability of the proposed NT-PEM is validated by evaluating the dynamic behavior of the MC during closing operation and comparing the results with 3D FEA analysis calculated using JMAG and experimental data obtained from an MC prototype (Figs. 16–18). Equations in Section V are solved using the TDM with $dt = 0.1$ ms. The analysis is conducted in the MATLAB environment using original scripts. The FE solution is obtained using the commercial 3D modeling software JMAG. Forces in the NT-PEM are calculated using both the change in inductance and energy, as discussed in Section VI. Both approaches provide good agreement with FE modeling results. This might be unexpected because the influence of the magnet is omitted when using the change in inductance to calculate the results. However, this can be explained by the fact that the contribution of the magnet to the force becomes significant only when the main air gap is extremely small. Therefore, the force is mainly determined by the coil current for most of the displacement range during the closing of the MC due to the large main air gap. This argument is supported by the fact that the shape of the electromagnetic force in Fig. 16 is similar to the shape of the coil current in Fig. 17. Though slight differences can be observed in the

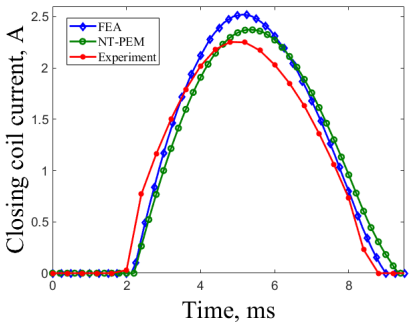


**FIGURE 17.** Closing coil current versus time during MC closing operation. Comparison of FEA, MEC, and experimental results.

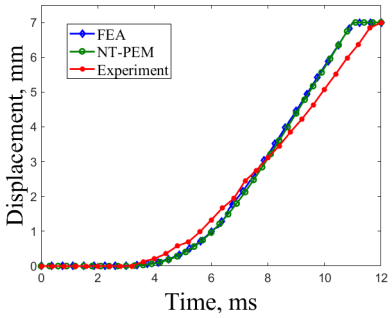


**FIGURE 18.** Displacement of the MC armature versus time during MC closing operation.

force calculation results, the displacement calculation results in Fig. 18 are almost identical for the FEA and the NT-PEM.

The differences between the model and experimental results in Figs. 17 and 18 are a consequence of the effects not taken into account by either model (e.g., eddy currents, coil energy loss, the temperature dependence of the magnetic parameters, manufacturing errors, and effects arising from mechanical collisions between the armature and stator). The amplitude of the current calculated using the NT-PEM is slightly more accurate compared to the FEA. On the other hand, the predicted total time until the current reaches zero is slightly longer. Nevertheless, the difference between the experimental and calculation results is between 5 and 10%, indicating that the proposed method is highly accurate. It should be emphasized that this is particularly remarkable because the proposed method not only solves quasi-static problems but also evaluates complete actuator dynamics in the time domain. Although the FE model is primarily used to determine the NT-PEM parameters in this study, further analysis of experimental data can be used to improve the accuracy of the method.

### B. MAGNET HOLDING FORCE IN A CLOSED STATE

An additional experiment is conducted during the closed state to evaluate the holding force produced by the magnet. In the FEA, both the closing and opening coil currents are kept at zero at the end of the closing operation, and the electromagnetic force due to the magnet alone is calculated.

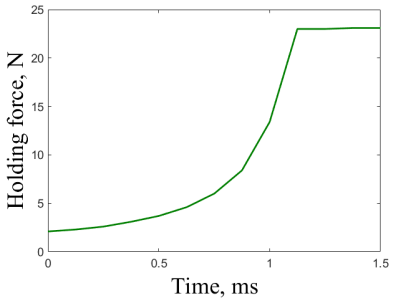


**FIGURE 19.** Increase in the electromagnetic force up to the magnet holding force as the armature reaches its final position at the end of the MC closing operation.

In the NT-PEM, the magnet holding force is calculated based on the consideration of path energies. Fig. 19 shows that the holding force of the magnet reaches 23.1 N in the FEA. The NT-PEM result is 22.9 N, a difference of less than 1%.

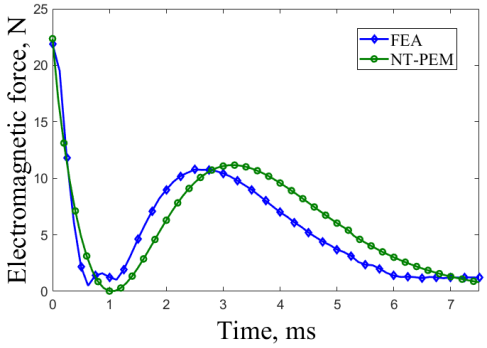


**FIGURE 20.** Electromagnetic force versus time during MC opening operation.

### C. OPENING OPERATION OF THE MC

The opening of the MC is studied in the same manner as the closing discussed in Section VII. During the opening operation, the direction of the opening current opposes that of the closing current, leading to the reversal of the sign of the coil mmf in Fig. 12 (c) and repulsion between the opening coil current and the main magnet. As discussed in Section VI, only the path energy method can be used to calculate the opening repulsive force in this MC. As the coil current increases at the beginning of opening operation, it decreases the attractive electromagnetic force produced by the magnet from the magnet holding force down to zero, as shown in Fig. 20. The force then becomes purely repulsive and increases as the coil current grows. However, it later starts decreasing because the distance between the coil and the magnet becomes too large. When the magnet holding force drops below a specific value, the energy stored in the opening spring during closing is released, accelerating the movement of the armature. Consequently, the overall dynamic behavior of the MC during opening operation is determined to a significant extent by the opening spring. This means less time is required to complete the opening operation, which

is important for preventing the welding of moving contacts with stationary ones. The difference between the FEA and NT-PEM force calculation results in Fig. 21 can be attributed to the difference in the current.

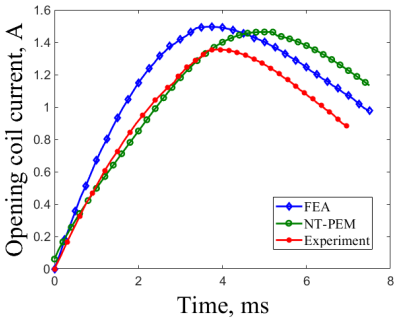


**FIGURE 21.** Opening coil current versus time during MC opening operation.

### D. MAGNET HOLDING FORCE IN A CLOSED STATE

The electromagnetic force during the opening is lower than that during the closing in Fig. 16 because of the lower supply current and higher magnet flux leakage. The latter is a consequence of flux redistribution in the MC magnetic circuit after the sign of the coil mmf is reversed. While only $\Phi_{ms}$ flux is attributed to magnet leakage during the closing operation, the analysis of ND-MEC flux distribution during the opening shows that almost half of the $\Phi_{c2s}$ flux circulates around the magnet without contributing to the linked flux. Simultaneously, the coil magnetic flux does not reach the side gap $R_{g2}$, taking shorter paths through $R_{g2s}$ directly to the stator wall. These effects occur only when the opening coil and the magnet are sufficiently far apart. As a result, the energy contributions of the air regions surrounding the armature are adjusted to account for these effects. Overall, the flux distribution in the ND-MEC during opening operation is clearly different from that during closing. This leads to the difference between the force curves in Figs. 16 and 20.

It should be mentioned that the inductances (50), (51), (54), and (55) are found to be most susceptible to numerical errors during TDM analysis. While the accuracy of the results for the opening operation is lower than that of the closing, the associated errors are still below 10%, meaning that this method can be reliably used for the proposed purposes.

## VIII. DISCUSSIONS AND FINAL REMARKS

### A. THE COMPUTATIONAL SPEED AND ACCURACY OF THE PROPOSED NT-PEM

#### 1) COMPUTATIONAL SPEED OF THE NT-PEM COMPARED WITH FE TIME-STEP ANALYSIS

The results presented in Section VII show good agreement between the FEA, NT-PEM, and experiment results, with the error not exceeding 10%. However, the proposed NT-PEM is significantly more computationally efficient than FEA. Table 5 shows that the proposed NT-PEM is faster than FEA of comparable accuracy. Moreover, even FEA with

**TABLE 5.** Computational time comparison between the NT-PEM and FEA of varying mesh refinement levels. Errors are computed in comparison with the experimental results.

| Analysis type | Time | Av. error, % | Time | Av. error, % | Time | Time Ratio |
|---|---|---|---|---|---|---|
| Operation | Closing | | Opening | | Complete | |
| NT-PEM | 4 s | 6 | 2.7 s | 8 | 6.7 s | 1 |
| FEA (30k*) | 40 min | 5 | 34 min | 7 | 74 min | 663 |
| FEA (9k) | 9 min | 13 | 7 min | 16 | 16 min | 143 |
| FEA (2k) | 4 min | 18 | 3 min | 22 | 7 min | 63 |

*"k" stands for a thousand elements

coarse mesh (i.e., a low number of elements) still requires a computational time that is more than 50 times longer due to non-linear transient analysis. Because the accuracy of FEA is proportional to the mesh refinement level and consequently to the computational time, the average error of fast FEA increases, exceeding 20% compared to the experiment results. Therefore, for FEA to provide better accuracy, the said ratio of computational time must exceed 500 times, requiring more than 1 h for a complete analysis to be conducted (see Table 5). This leads to significant computational costs when employing FEA for PM-type MCs. In contrast, the complete operating cycle is computed in 6.7 seconds using the NT-PEM, allowing the cost-efficient analysis and optimization of numerous designs. In addition, relationships between its input parameters can easily be programmed, and optimization algorithms can be conveniently incorporated into the analysis because NT-PEM does not require specialized software for its implementation.

#### 2) ACCURACY OF THE NT-PEM COMPARED TO THE TRADITIONAL MEC METHODS

The high accuracy of the NT-PEM is achieved due to the high accuracy of the individual components, such as the proposed ND-MEC, and their combination, e.g., the ND-MEC combined with the TDM. As mentioned in Section II, the accuracy of traditional MEC methods decreases when the effects of non-linear material properties and complicated magnetic flux distributions are significant. This problem is addressed by introducing several improvements in the ND-MEC method.

The accuracy of the traditional MEC is enhanced by incorporating material non-linearities into the analysis. This is achieved by employing an algorithm to estimate the working point on the $B$–$H$ curve for the flux guide steel, as discussed in Section III. This algorithm uses the rational function $\mu_r(H)$ for core permeability correction, which allows the estimation of the variation in core permeability with the current and the position of the armature. The high accuracy of the approximation proves the applicability of the rational function in the ND-MEC model. It should be mentioned that the overall computational time of the TDM depends on the number of iterations in the core permeability correction routine, meaning that further optimization of this technique could reduce the time required for convergence and decrease the overall computational time of the model even further.

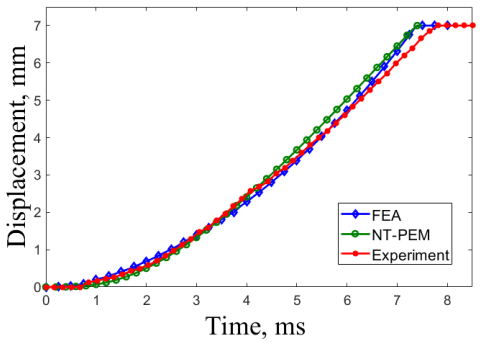


**FIGURE 22.** Displacement of the MC armature versus time during MC opening operation.

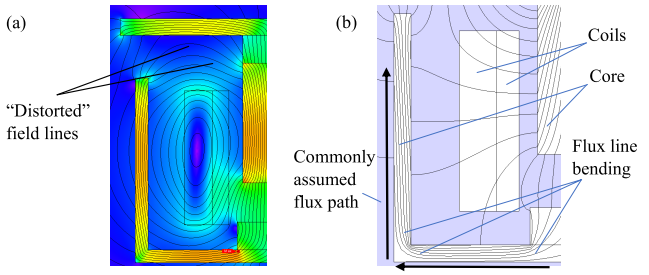


**FIGURE 23.** 2D magnetic field lines in the MC with strong magnetic fields. (a) Distortion of flux lines near the core regions due to magnetic saturation effects. (b) Bending of flux lines near the corners and interior sections of the flux guide forming elliptical paths.

A new approach to modeling stray fluxes is proposed. It is assumed that stray fluxes follow elliptical paths outside core regions, providing a concise approach to the calculation of associated reluctances. The accuracy of this approach is first verified using a simple model in Section III and then using a complete version of the ND-MEC, in which it successfully modeled the complicated 3D flux distribution of an MC magnetic circuit. This MC design is particularly suitable for illustrating the applicability of the new stray flux evaluation method because a significant portion of its total flux does flow outside the flux guide region.

The combination of the iterative algorithm for calculating the non-linear core permeability with the elliptical path approach in the proposed structure of the ND-MEC addresses the drawbacks of traditional MEC methods, expanding the applicability of MEC analysis by improving its accuracy and extending the number of possible problems to which it can be applied.

### *B. ADVANTAGES OF THE PROPOSED ELLIPTICAL FUNCTION FOR STRAY PATH RELUCTANCE ESTIMATION IN ND-MEC*

#### 1) MODELING FLUX PATHS WITH ARBITRARY SHAPES AS ELLIPTICAL ARCS

This study proposes a novel approach to estimating the lengths of stray flux paths using the elliptical function introduced in Section III. The main assumption in this proposed approach is that the shape of a stray flux path can be represented by the arc of an ellipse. Therefore, the overall shape of a flux loop can be considered as being pieced together from multiple elliptical arcs, as illustrated in Fig. 23. The validity of this assumption can be tested by considering the field lines in core regions, which are commonly represented by straight-line paths in MEC models. Fig. 23 (b) shows that field lines bend near the corners of the core, producing corner saturation, a well-known local effect. This results in the slight bending of the lines within the core. Consequently, field lines follow elliptical paths that can be treated as the arcs of an imaginary ellipse with a very long focal distance, as discussed in Section III. One consequence of this observation is that the flux paths in the core in Figs. 23 (a) and (b) are longer than the paths calculated using straight-line approximation. However, this effect is rather small and can generally be neglected without any effect on the accuracy of the model. Nevertheless, this shows that, in principle, elliptical path representation can explain both flux line bending and local core saturation effects. Similarly, when a flux line with a small tangential component of flux density $B_t$ approaches the air gap, it passes through almost undisturbed, forming a near-straight line path due to the continuity of the magnetic flux density [59]–[61]. On the other hand, lines that bend more inside the core tend to deviate from straight-line paths to follow elliptical paths outside the core region. Therefore, a complete loop is indeed a combination of multiple elliptical arcs that are separated due to non-homogeneities in the medium (e.g., by the presence of regions with different magnetic properties and sources of magnetic excitation). Therefore, this example illustrates that the proposed elliptical function is able to model all cases typically used in main and leakage path modeling while not requiring an assumption about the exact shape of the flux path to be made.

#### 2) POTENTIAL FOR THE FURTHER GENERALIZATION USING *K*-ELLIPSES

It is possible for field lines to be significantly disturbed by strong electric currents and the high saturation of ferromagnetic regions, as shown in Fig. 23 (a). In FE analysis, this is reflected by the non-homogeneous distribution of magnetic vector potential. For the elliptical path method presented in this study, this disturbance implies the existence of multiple focal points for the same elliptical arc representing a bent flux path. Therefore, the path follows an arc of a $k$-ellipse [62], [63]. The shape of $k$-ellipses can be distorted more than that of 2-ellipses due to the additional foci, which represent sources of distortion in the magnetic field. The elliptical path approach has the potential to model all flux paths with arbitrary shapes and complexity if $k$-ellipse mathematics is used, which could represent a generalized modeling approach applicable but not limited to the ND-MEC method. However, for engineering purposes, simplified versions (e.g., the 2-foci ellipse method proposed in this paper) should be implemented.

### C. ADVANTAGES OWING TO THE ABILITY TO MODEL MAGNETIC FLUX AND ENERGY DISTRIBUTION

#### 1) ADVANTAGES OF ND-MEC IN TERMS OF STRAY AND LEAKAGE FLUX MODELING

The ability to analyze flux distributions with high accuracy is an important feature of the ND-MEC method. This analysis illustrates that a considerable portion of the flux avoids the flux guide in the vicinity of the magnet in an MC with large air gaps in its open state. This includes not only magnet leakage but also a large fraction of the main flux flowing directly to the armature upper plate, avoiding the magnet and armature pole sections. The region surrounding the side air gaps is also prone to flux spread. An analysis of the flux distribution of these two sections requires the application of the novel elliptical function proposed in this paper. Being able to analyze stray flux paths and the underlying reasons for their high permeance increases the possibility of optimizing the flux guide by focusing the main flux through minimizing stray fluxes. This is possible because stray paths are primarily determined by the MC flux guide geometry.

#### 2) ADVANTAGES OF THE PATH ENERGY ANALYSIS FOR THE ACCURATE ESTIMATION OF ELECTROMAGNETIC FORCES

The most important consequence of flux distribution analysis is the ability to estimate the extent to which stray flux path energy contributes to the output force of the MC. This is best illustrated by analyzing the stray flux$R_{c2s}$ in the side air gap region. Magnetic flux through this region is very high, and it changes rapidly due to armature motion. While $R_{c2s}$ reluctance does not directly depend on displacement, its flux changes due to the redistribution of magnetic fluxes in the branches of the ND-MEC with armature displacement. Changes in magnetic flux indicate that magnetic energy varies with armature displacement, contributing to the output force in (70). On the other hand, stray reluctances contribute to the derivative of inductance as in (67), affecting the calculation of force. Hence, stray reluctances play a significant role in the calculation of force using either the change in inductance or the change in energy. However, force calculation using the energy-change method must be corrected for the misalignment between the force and displacement vectors using the coefficient $k_w$, which accounts for the bending of the flux tubes in (72)–(74). The combination of the path energy method and the proposed coefficient results in the highly accurate calculation of force in all studied regimes. This is particularly important for MC performance analysis because the path energy method discussed in Section VI allows the electromagnetic forces arising from the interaction between the coils and the magnet to be calculated. Otherwise, the calculation of electromagnetic forces is limited to cases where the forces are reactive or where the contribution of one of the sources (i.e., the coils or magnet) can be ignored.

### D. ADVANTAGES OF THE NT-PEM FOR THE COMPLETE EVALUATION OF THE DYNAMICS OF ELECTRICAL MACHINES

#### 1) OVERCOMING THE QUASI-STATIC LIMITATIONS OF THE MEC METHOD BY INTEGRATING THE TDM

Although the ND-MEC method is able to represent the flux distribution and calculate energy with high accuracy, the NT-PEM is required to realize the full potential of the methodology proposed in this paper. The ND-MEC approach, and MEC methods in general, are in principle analogous to quasi-static FEA. However, quasi-static representation only allows dynamics to be assessed in a limited number of cases. For instance, the analysis of the periodic steady-state performance of rotating machines allows guiding equations to be formulated in terms of relative angle rather than time or position, resulting in a possibility to calculate forces analytically [19], [23]. Outside of isolated cases such as this, however, MEC methods generally do not allow dynamics to be evaluated. Therefore, much of the research that has proposed new MECs still requires the use of the FEM to assess performance in the time domain [23], [25]. In addition, the relationship between time, speed, and displacement for linear actuators such as an MC is generally unknown, unlike the relationship between frequency, angular velocity, and the rotor positions of a rotating machine. This means any analysis of the dynamics of the linear motion of the MC is much more complex. Therefore, the ability to evaluate the non-linear dynamics of an MC is a crucial feature of the proposed NT-PEM, which illustrates its advantages over other methods. The advantages of the ND-MEC can be extended to the time domain via the NT-PEM, which is based on the path energy method proposed in Section VI, which allows the highly accurate calculation of force because the magnetic and mechanical non-linearities of the ND-MEC are carefully considered. The addition of correction coefficients further increases the accuracy of the proposed method, accounting for the 3D nature of the magnetic field distribution in an MC.

#### 2) MODELING NON-LINEAR AND NON-PERIODIC DYNAMICS

The validity of the NT-PEM is proven by the accurate calculation of the non-linear performance characteristics of the MC shown in Figs. 16–22. It should be stressed that an important advantage of the proposed method is that is can be used for cases that involve multiple excitation sources. This study shows that the NT-PEM can be employed to calculate both the attractive and repulsive forces between the coils and the PM. Moreover, unlike many other models dealing with coil-magnet force calculation, the calculation of force in the proposed method takes into account the actual geometry of the magnetic circuit and the PM without requiring assumptions or simplifications. The provided solution is more general than approaches that require the construction of polynomial

representations of forces and flux linkages. The correction coefficient used in Section VI has an exact physical meaning and is calculated based on ND-MEC parameters. This allows the NT-PEM to maintain generality when applied to cases other than the studied MC.

The above discussion indicates that the proposed NT-PEM can be used for the design and analysis of various electrical machines, considerably extending the area of applicability of the method. While the electrical and mechanical equations and the corresponding ND-MEC need to be specific to the electrical machine under analysis, the overall structure of the NT-PEM in Fig. 15 remains unchanged. This illustrates the great potential for the use of the NT-PEM in the high-speed, highly accurate, and low-cost analytical analysis of electrical machines. It is also worth noting that this method is not necessarily limited to electrical machine analysis and design, as discussed in the next sub-section.

### *E. POTENTIAL APPLICATION OF THE NT-PEM IN MULTIDISCIPLENARY RESEARCH AREAS*

#### 1) THE IMPORTANCE OF NON-LINEAR COUPLED ANALYSIS IN MULTIDISCIPLINARY RESEARCH

As previously discussed, most energy conversion devices, including but not limited to electrical machines, are complex systems where multiple physical aspects are coupled together. Decoupling remains a common method of modeling physical reality in engineering design. Due to the complexity of the underlying physics, engineering models tend to approximate and simplify inherently coupled problems, often by applying empirical techniques and models based on prior experience. The electrical–magnetic–mechanical problem studied in this paper is a well-known example that is rarely solved accurately for each of its three aspects simultaneously [64]. Nevertheless, coupling is necessary to model the dynamics of an MC in the time domain. A similar argument can be made for many emerging fields where decoupling techniques are not known or cannot be readily implemented. For instance, smart materials, which hold enormous potential for use in novel devices, inherently couple several physical aspects. The best-known examples are piezoelectric materials, which exhibit electrostatic-mechanical coupling [65], shape memory alloys (SMAs), in which a mechanical response is triggered by temperature [66], and ferromagnetic shape memory alloys (FSMAs or MSMs), which exhibit magneto-mechanical coupling [67]. The application of decoupled analysis techniques to these materials can result in a non-realistic representation of their properties, potentially leading to the neglect of many important properties or the failure to realize the full potential of new technologies. Moreover, many smart materials, especially those exhibiting a shape memory effect, have non-linear magneto-mechanical or thermal-mechanical characteristics with distinct hysteresis [68]–[70]. This makes designing novel devices based on smart materials extremely challenging.

#### 2) BRIDGING METHODOLOGICAL DIFFERENCES FOR EMERGING TECHNOLOGIES

Although novel design and analysis techniques are required for emerging technologies, a challenge that needs to be overcome is the considerable methodological differences that exist between the approaches used in different fields. For instance, models proposed for smart materials are typically characterized by their extreme mathematical complexity, limiting their compatibility with engineering design techniques [71]. An alternative approach based on the accurate modeling of only those properties of a new material directly related to engineering applications has recently been proposed for MSM actuators [72], [73]. However, this method relies on FEA, making it computationally expensive. Similarly, FEA has been used to analyze complex structures associated with porous materials and foams [74], [75]. However, FEM software is usually tailored for specific purposes, which acts as an obstacle for more generalized applications.

#### 3) APPLICABILITY OF THE NT-PEM IN MULTIDISCIPLENARY RESEARCH

This study illustrates that equivalent circuit models can be employed in multidomain analysis via the NT-PEM. As proven by this study, the NT-PEM allows the analysis of coupled problems that exhibit non-linear dynamic behavior, something which is essential for multidisciplinary research. The ability to simplify differential equations via the TDM allows any problem to be formulated using a consistent engineering language, producing a comprehensive analysis and design model that can be rapidly solved with a computer. The ND-MEC method outlined in this study proves that it is possible to represent the complicated 3D behavior of physical fields with lumped parameters when the characteristics of these fields are carefully considered (e.g., the application of an elliptical function for magnetic paths). This approach resembles homogenization techniques, which are widely used in multidisciplinary research [76]–[78]. However, the NT-PEM method allows the analysis of not only particular components (e.g., novel materials and their behavior) of a device but also the device as a whole and its performance under real conditions. This is achieved by localizing the complexity related to the geometrical features, non-linearities, and non-homogeneities of the material properties in lumped parameters [3], [60], such as the reluctances of the ND-MEC, allowing the method to be generally applicable to a wide range of multidisciplinary problems.

#### 4) ADVANTAGES OF THE PROPOSED NT-PEM COMPARED TO TRADITIONAL METHODS

An example of a field where equivalent circuit methods have already demonstrated some success is piezoelectric energy harvesting [79], [80]. However, complications arise due to the complexity of the electrostatic-mechanical equations. The traditional coupling approach for interrelated electrical and

mechanical problems is related to the implementation of electromechanical circuits [81], [82]. This approach is based on matching the energy flow throughout the harvester [83]. Therefore, the equivalent circuit method provides a unified representation of multi-domain systems in the same way the ND-MEC is utilized in the NT-PEM. However, while the properties of piezoelectric materials can be treated as linear, the frequency response and dynamic behavior of various smart materials exhibit strongly non-linear behavior [84], [85]. Therefore, an accurate method for analyzing non-linear dynamics, such as the proposed NT-PEM, is needed to represent the behavior of complex multiphysics systems with high accuracy.

## IX. CONLCUSIONS

This paper proposes the NT-PEM, a novel analytical method for the analysis of the dynamic performance of electrical machines that is applied to the analysis of PM-type MCs. The goal of accurately evaluating the overall dynamics of the MC is achieved by incorporating several novel approaches into the NT-PEM. These approaches address the common drawbacks of traditional analytical methods and are outlined below.

1. The MC modeled in this study, which has a PM and large air gaps, is characterized by two types of non-linearity, one owing to the non-linear magnetic properties of the core, the other to the non-linear dependence of stray-path reluctances on armature displacement. These effects mean that traditional MEC methods cannot be employed to analyze PM-type MCs, necessitating the use of time-consuming and computationally expensive FEA. Hence, one of the significant contributions of this paper is that the proposed ND-MEC method incorporates solutions to both of these problems. This is achieved by proposing two novel techniques which significantly increase the accuracy of the analysis. First, an iterative algorithm for core permeability correction using a rational approximation of the experimental $B$–$H$ curve is proposed to account for material non-linearities. Second, stray path reluctances are introduced and calculated using an elliptical function, which accurately accounts for both the distribution of stray fluxes and their dependence on armature position. The accuracy of the ND-MEC is verified by comparing its performance with 3D FEA in Section III.

2. Traditional methods for the calculation of electromagnetic force in electrical machines commonly consider linear or periodic cases, for which an analytical solution can be obtained. However, the dynamics of the studied MC are both non-linear and non-periodic, limiting the use of traditional methods. This problem is addressed by first applying an inductance-change method in Section VI, which accounts for non-linear effects. However, this approach is still limited by the number of excitation sources. In order to address this problem, a novel path energy method, which builds on the ability of the ND-MEC to model dynamic changes in the magnetic field distribution, is proposed in Section VI. This extends the applicability of the ND-MEC to complex electromagnetic force calculations that incorporate non-linear effects and multiple excitation sources (i.e., both coils and the PM).

3. The non-linearity and non-periodicity of the performance characteristics of PM-type MCs means that analyzing the overall dynamics using traditional methods is impossible. This problem is solved in this study using the NT-PEM method, which combines the ND-MEC with the TDM and the path energy method to calculate the force. This means it is possible to analyze non-linear dynamics with high accuracy. The method is verified by comparing its performance to 3D FEA and experimental results obtained from an MC prototype, proving its applicability and accuracy. The proposed method is fast, accurate, and computationally inexpensive, which gives it an advantage over time-consuming and computationally expensive FEA when many designs need to be evaluated and optimized.

4. The potential for the NT-PEM to model coupled multi-domain problems, such as the electro-magnetic-mechanical coupled problem studied in this paper, makes this method very promising for a wider range of multiphysics problems. First, other types of electrical machines that utilize both linear and rotational motion can be analyzed. Second, novel smart-material-based applications, which inherently couple multi-physics effects, can be analyzed using the proposed method. This is very promising due to the ability to connect multiple domains in a single physically valid equivalent circuit, which can be easily tailored for a particular problem. Circuit parameters can be easily adjusted, unlike in FEA, which is accurate but not sufficiently flexible when applied in emerging fields for which a sufficiently reliable methodology has yet to be developed.

## REFERENCES

[1] J. Zhao, W. Fu, Y. Zheng, Z. Chen, and Y. Wang, "Comparative study of modular-stator and conventional outer-rotor flux-switching permanent-magnet motors," *IEEE Access*, to be published.

[2] T. Merzouki, A. Duval, and T. Ben Zineb, "Finite element analysis of a shape memory alloy actuator for a micropump," *Simul. Model. Pract. Theory*, vol. 27, pp. 112–126, Sep. 2012.

[3] H.-K. Yeo, H.-J. Park, J.-M. Seo, S.-Y. Jung, J.-S. Ro, and H.-K. Jung, "Electromagnetic and thermal analysis of a surface-mounted permanent-magnet motor with overhang structure," *IEEE Trans. Magn.*, vol. 53, no. 6, Jun. 2017, Art. no. 8203304.

[4] W. Zhao, F. Xing, X. Wang, T. A. Lipo, and B.-I. Kwon, "Design and analysis of a novel PM-assisted synchronous reluctance machine with axially integrated magnets by the finite-element method," *IEEE Trans. Magn.*, vol. 53, no. 6, Jun. 2017, Art. no. 8104104.

[5] R. Xu, C. Bouby, H. Zahrouni, T. B. Zineb, H. Hu, and M. Potier-Ferry, "3D modeling of shape memory alloy fiber reinforced composites by multiscale finite element method," *Compos. Struct.*, vol. 200, pp. 408–419, Sep. 2018.

[6] Y. Sun, B. Su, and X. Sun, "Optimal design and performance analysis for interior composite-rotor bearingless permanent magnet synchronous motors," *IEEE Access*, vol. 7, pp. 7456–7465, 2019.

[7] O. Zienkiewicz, R. Taylor, and J. Z. Zhu, *The Finite Element Method: Its Basis and Fundamentals*, 6th ed. Amsterdam, The Netherlands: Elsevier, 2005.

[8] D. Lee, J.-Y. Song, M.-K. Seo, H.-C. Jung, J.-W. Kim, and S.-Y. Jung, "Development of differing extent mesh adaptive direct search applied for optimal design of spoke-type PMSM," *IEEE Trans. Magn.*, vol. 54, no. 11, Jul. 2018, Art. no. 8205905.

[9] G.-J. Park, B. Son, S. Seo, J.-H. Lee, Y.-J. Kim, and S.-Y. Jung, "Compensation strategy of the numerical analysis in frequency domain on induction motor considering magnetic flux saturation," *IEEE Trans. Magn.*, vol. 54, no. 3, Mar. 2018, Art. no. 8201604.

[10] H.-J. Park, H.-K. Jung, S.-Y. Jung, Y.-H. Chae, and D.-K. Woo, "Field reconstruction method in axial flux permanent magnet motor with overhang structure," *IEEE Trans. Magn.*, vol. 53, no. 6, Jun. 2017, Art. no. 8201304.

[11] J.-W. Kwon and B.-I. Kwon, "Investigation of dual-stator spoke-type Vernier machine for EV application," *IEEE Trans. Magn.*, vol. 54, no. 11, Jul. 2018, Art. no. 8206505.

[12] Y.-C. Wu and B.-S. Jian, "Magnetic field analysis of a coaxial magnetic gear mechanism by two-dimensional equivalent magnetic circuit network method and finite-element method," *Appl. Math. Model.*, vol. 39, no. 19, pp. 5746–5758, 2015.

[13] G.-J. Park, J.-S. Kim, B. Son, and S.-Y. Jung, "Optimal design of PMa-synRM for an electric propulsion system considering wide operation range and demagnetization," *IEEE Trans. Appl. Supercond.*, vol. 28, no. 3, Apr. 2018, Art. no. 5205804.

[14] S. D. Sudhoff, *Power Magnetic Devices: A Multi-Objective Design Approach*, 1st ed. Hoboken, NJ, USA: Wiley, 2014.

[15] A. B. Yildiz, "Electrical equivalent circuit based modeling and analysis of direct current motors," *Int. J. Elect. Power Energy Syst.*, vol. 43, no. 1, pp. 1043–1047, 2012.

[16] D. Zheng, D. Wang, S. Li, H. Zhang, L. Yu, and Z. Li, "Electromagnetic-thermal model for improved axial-flux eddy current couplings with combine rectangle-shaped magnets," *IEEE Access*, vol. 6, pp. 26383–26390, 2018.

[17] W. Cai, C. Gu, and X. Hu, "Analysis and design of a permanent magnet bi-stable electro-magnetic clutch unit for in-wheel electric vehicle drives," *Energies*, vol. 8, no. 6, pp. 5598–5612, 2015.

[18] D. Wang, X. Du, D. Zhang, and X. Wang, "Design, optimization, and prototyping of segmental-type linear switched-reluctance motor with a toroidally wound mover for vertical propulsion application," *IEEE Trans. Ind. Electron.*, vol. 65, no. 2, pp. 1865–1874, Feb. 2018.

[19] H.-S. Seol, J. Lim, D.-W. Kang, J.-S. Park, and J. Lee, "Optimal design strategy for improved operation of IPM BLDC motors with low-resolution Hall sensors," *IEEE Trans. Ind. Electron.*, vol. 64, no. 12, pp. 9758–9766, Dec. 2017.

[20] J.-Y. Song, J. H. Lee, D.-W. Kim, Y.-J. Kim, and S.-Y. Jung, "Analysis and modeling of concentrated winding variable flux memory motor using magnetic equivalent circuit method," *IEEE Trans. Magn.*, vol. 53, no. 6, Jun. 2017, Art. no. 8102704.

[21] D.-K. Lim, S.-Y. Jung, K.-P. Yi, and H. K. Jung, "A novel sequential-stage optimization strategy for an interior permanent magnet synchronous generator design," *IEEE Trans. Ind. Electron.*, vol. 65, no. 2, pp. 1781–1790, Feb. 2018.

[22] J. H. Lee, J.-Y. Song, D.-W. Kim, J.-W. Kim, Y.-J. Kim, and S.-Y. Jung, "Particle swarm optimization algorithm with intelligent particle number control for optimal design of electric machines," *IEEE Trans. Ind. Electron.*, vol. 65, no. 2, pp. 1791–1798, Feb. 2018.

[23] L. Guo, C. Xia, H. Wang, Z. Wang, and T. Shi, "Improved equivalent magnetic network modeling for analyzing working points of PMs in interior permanent magnet machine," *J. Magn. Magn. Mater.*, vol. 454, pp. 39–50, May 2018.

[24] H.-J. Bak, J.-S. Ro, T.-K. Chung, and H.-K. Jung, "Characteristics analysis and design of a novel magnetic contactor for a 220 V/85 A," *IEEE Trans. Magn.*, vol. 49, no. 11, pp. 5498–5506, Nov. 2013.

[25] M.-F. Hsieh and Y.-C. Hsu, "A generalized magnetic circuit modeling approach for design of surface permanent-magnet machines," *IEEE Trans. Ind. Electron.*, vol. 59, no. 2, pp. 779–792, Feb. 2012.

[26] J. M. Seo, I. S. Jung, H. K. Jung, and J. S. Ro, "Analysis of overhang effect for a surface-mounted permanent magnet machine using a lumped magnetic circuit model," *IEEE Trans. Magn.*, vol. 50, no. 5, May 2014, Art. no. 8201207.

[27] H.-J. Park, S.-H. Kim, J.-S. Ro, and H.-K. Jung, "Analysis and design of separated permanent magnet actuator for 225AF molded case circuit breaker," in *Proc. 7th Int. Conf. Elect. Mach. Syst. (ICEMS)*, Oct. 2014, pp. 2888–2891.

[28] A. Torres-Perez, A. Hassan, S. Kaczmarczyk, and P. Picton, "Active vibration control using mechanical and electrical analogies," *J. Phys. Conf. Ser.*, vol. 721, no. 1, 2016, Art. no. 012013.

[29] D. Tufano and Z. Sotoudeh, "Exploring the entropy concept for coupled oscillators," *Int. J. Eng. Sci.*, vol. 112, pp. 18–31, Mar. 2017.

[30] Y. Tang, J. J. H. Paulides, and E. A. Lomonova, "Analytical modeling of flux-switching in-wheel motor using variable magnetic equivalent circuits," *ISRN Automot. Eng.*, vol. 2014, Jan. 2014, Art. no. 530260. doi: 10.1155/2014/530260.

[31] D. Faustner, W. Kemmetmüller, and A. Kugi, "Magnetic equivalent circuit modeling of a saturated surface-mounted permanent magnet synchronous machine," *IFAC-PapersOnLine*, vol. 48, no. 1, pp. 360–365, 2015.

[32] J. Bao, B. L. J. Gysen, and E. A. Lomonova, "Hybrid analytical modeling of saturated linear and rotary electrical machines: Integration of Fourier modeling and magnetic equivalent circuits," *IEEE Trans. Magn.*, to be published.

[33] S. A. Randi, R. Benlamine, F. Dubas, and C. Espanet, "Semi-analytical method based on magnetic equivalent circuit in EV and HEV applications," *Mediterr. J. Model. Simul.*, vol. 1, pp. 1–12, 2014.

[34] P. Diez and J. P. Webb, "A rational approach to $B - H$ curve representation," *IEEE Trans. Magn.*, vol. 52, no. 3, Mar. 2016, Art. no. 7203604.

[35] J. M. Kokernak and D. A. Torrey, "Magnetic circuit model for the mutually coupled switched-reluctance machine," *IEEE Trans. Magn.*, vol. 36, no. 2, pp. 500–507, Mar. 2000.

[36] C. A. Vaithilingam, N. Misron, M. R. Zare, I. Aris, and M. H. Marhaban, "Computation of electromagnetic torque in a double rotor switched reluctance motor using flux tube methods," *Energies*, vol. 5, no. 10, pp. 4008–4026, 2012.

[37] A. Stuikys and J. Sykulski, "Rapid multi-objective design optimisation of switched reluctance motors exploiting magnetic flux tubes," *IET Sci. Meas. Technol.*, vol. 12, no. 2, pp. 223–229, 2018.

[38] A. Stuikys, M. Rotaru, and J. K. Sykulski, "A refined approach exploiting tubes of flux for analysis of linear switched reluctance motors," *Int. J. Appl. Electromagn. Mech.*, vol. 51, pp. S13–S21, Apr. 2016.

[39] B. Sheikh-Ghalavand, S. Vaez-Zadeh, and A. H. Isfahani, "An improved magnetic equivalent circuit model for iron-core linear permanent-magnet synchronous motors," *IEEE Trans. Magn.*, vol. 46, no. 1, pp. 112–120, Jan. 2010.

[40] H.-K. Yeo, D.-K. Lim, D.-K. Woo, J.-S. Ro, and H.-K. Jung, "Magnetic equivalent circuit model considering overhang structure of a surface-mounted permanent-magnet motor," *IEEE Trans. Magn.*, vol. 51, no. 3, Mar. 2015, Art. no. 8201004.

[41] W. Robertson, B. Cazzolato, and A. Zander, "Axial force between a thick coil and a cylindrical permanent magnet: Optimizing the geometry of an electromagnetic actuator," *IEEE Trans. Magn.*, vol. 48, no. 9, pp. 2479–2487, Sep. 2012.

[42] J. L. G. Janssen, J. J. H. Paulides, E. A. Lomonova, and A. J. A. Vandenput, "Analysis of a variable reluctance permanent magnet actuator," in *Proc. IEEE Ind. Appl. Annu. Meeting*, Sep. 2007, pp. 502–509.

[43] S. I. Babic and C. Akyel, "Magnetic force calculation between thin coaxial circular coils in air," *IEEE Trans. Magn.*, vol. 44, no. 4, pp. 445–452, Apr. 2008.

[44] R. Ravaud, G. Lemarquand, S. Babic, V. Lemarquand, and C. Akyel, "Cylindrical magnets and coils: Fields, forces, and inductances," *IEEE Trans. Magn.*, vol. 46, no. 9, pp. 3585–3590, Sep. 2010.

[45] W. Robertson, B. Cazzolato, and A. Zander, "A simplified force equation for coaxial cylindrical magnets and thin coils," *IEEE Trans. Magn.*, vol. 47, no. 8, pp. 2045–2049, Aug. 2011.

[46] M. B. Villarino. (2005). *Ramanujan's Perimeter of an Ellipse*. Accessed: Dec. 4, 2018. [Online]. Available: https://arxiv.org/abs/math/0506384

[47] S. J. Chapman, *Electric Machinery Fundamentals*, 5th ed. New York, NY, USA: McGraw-Hill, 2012.

[48] K. A. Hoffmann and S. T. Chiang, *Computational Fluid Dynamics for Engineers*, 4th ed. Wichita, KS, USA: Engineering Education System, 1993.

[49] J.-S. Rho, C.-H. Lee, and H.-K. Jung, "Characteristic analysis and design of a small size rotary ultrasonic motor using the cutting method," *Int. J. Appl. Electromagn. Mech.*, vol. 28, no. 4, pp. 469–500, 2008.

[50] D.-J. Cho, D.-K. Woo, J.-S. Ro, T.-K. Chung, and H.-K. Jung, "Novel electromagnetic actuator using a permanent magnet and an inter-locking mechanism for a magnetic switch," *IEEE Trans. Magn.*, vol. 49, no. 5, pp. 2229–2232, May 2013.

[51] L. Nagy, T. Szabó, and E. Jakab, "Electro-dynamical modeling of a solenoid switch of starter motors," *Procedia Eng.*, vol. 48, no. 1, pp. 445–452, 2012.

[52] S.-A. Yin and C.-T. Chi, "Energy distribution analysis in the closing process of contactor," in *Proc. IEEE Power Energy Soc. Gen. Meeting*, Jul. 2009, pp. 1–7.

[53] C. T. Chi, "Design and implementation of a new permanent magnet AC contactor with colenoid actuator," *WSEAS Trans. Circuits Syst.*, vol. 7, no. 11, pp. 942–954, 2008.
[54] X. Xue, K. W. E. Cheng, and Z. Zhang, "Model, analysis, and application of tubular linear switched reluctance actuator for linear compressors," *IEEE Trans. Ind. Electron.*, vol. 65, no. 12, pp. 9863–9872, Dec. 2018.
[55] Y.-S. Kwon and W.-J. Kim, "Electromagnetic analysis and steady-state performance of double-sided flat linear motor using soft magnetic composite," *IEEE Trans. Ind. Electron.*, vol. 64, no. 3, pp. 2178–2187, Mar. 2017.
[56] Z. Li, D. Wang, and D. Zheng, "Accurate prediction and analysis of electromagnetic fields and forces in flux-focusing eddy current coupling with double slotted conductor rotors," *IEEE Access*, vol. 6, pp. 37685–37699, 2018.
[57] G. P. Widdowson, "Design optimization of permanent magnet actuators," Ph.D. dissertation, Univ. Sheffield, Sheffield, England, 1992.
[58] J. S. Kim, D. W. Kim, G.-J. Park, Y. J. Kim, and S. Y. Jung, "Analysis and design of SPM type variable flux memory motor considering demagnetization characteristic of permanent magnet," *IEEE Trans. Appl. Supercond.*, vol. 28, no. 3, pp. 1–5, Apr. 2018.
[59] M. H. Nayfeh and M. K. Brussel, *Electricity and Magnetism*. New York, NY, USA: Wiley, 1985.
[60] N. Gabdullin and S. H. Khan, "Study of non-homogeneity of magnetic field distribution in single-crystal Ni–Mn–Ga magnetic shape memory element in actuators due to its anisotropic twinned microstructure," *IEEE Trans. Magn.*, vol. 53, no. 3, Mar. 2017, Art. no. 4900108.
[61] I. Sevostianov and M. Kachanov, "On discontinuities of thermal, electric and diffusion fluxes at interfaces of different materials," *Int. J. Eng. Sci.*, vol. 102, pp. 1–3, May 2016.
[62] J. Nie, P. A. Parrilo, and B. Sturmfels, "Semidefinite representation of the k-ellipse," in *Algorithms in Algebraic Geometry*. New York, NY, USA: Springer, 2007, pp. 117–132.
[63] J. C. Maxwell and P. M. Harman, *The Scientific Letters and Papers of James Clerk Maxwell*. Cambridge, U.K.: Cambridge Univ. Press, 1990.
[64] Y. Xing and B. Liu, "A differential quadrature analysis of dynamic and quasi-static magneto-thermo-elastic stresses in a conducting rectangular plate subjected to an arbitrary variation of magnetic field," *Int. J. Eng. Sci.*, vol. 48, no. 12, pp. 1944–1960, Dec. 2010.
[65] H. Li, Y. Li, T. Cheng, X. Lu, H. Zhao, and H. Gao, "A symmetrical hybrid driving waveform for a linear piezoelectric stick-slip actuator," *IEEE Access*, vol. 5, pp. 16885–16894, 2017.
[66] N. Sakoh, T. Todaka, and M. Enokizono, "Magnetic properties of bilayer ferromagnetic shape memory ribbons," *IEEE Trans. Magn.*, vol. 50, no. 4, Apr. 2014, Art. no. 2501304.
[67] H. Yaguchi and K. Sasaki, "New type of magnetic actuator system for inspection in a complex pipe," *IEEE Trans. Magn.*, vol. 49, no. 7, pp. 3905–3908, Jul. 2013.
[68] M. H. Ghayesh and H. Farokhi, "Nonlinear behaviour of electrically actuated microplate-based MEMS resonators," *Int. J. Eng. Sci.*, vol. 71, pp. 137–155, Oct. 2013.
[69] K. F. Wang and B. L. Wang, "Non-linear flexoelectricity in energy harvesting," *Int. J. Eng. Sci.*, vol. 116, pp. 88–103, Jul. 2017.
[70] L. Riccardi, D. Naso, H. Janocha, and B. Turchiano, "A precise positioning actuator based on feedback-controlled magnetic shape memory alloys," *Mechatronics*, vol. 22, no. 5, pp. 568–576, Aug. 2012.
[71] J. Wang, Z. Moumni, W. Zhang, and W. Zaki, "A thermomechanically coupled finite deformation constitutive model for shape memory alloys based on Hencky strain," *Int. J. Eng. Sci.*, vol. 117, pp. 51–77, Aug. 2017.
[72] T. Schiepp, M. Maier, E. Pagounis, A. Schlüter, and M. Laufenberg, "FEM-simulation of magnetic shape memory actuators," *IEEE Trans. Magn.*, vol. 50, no. 2, Feb. 2014, Art. no. 7024504.
[73] N. Gabdullin and S. H. Khan, "Electromagnetic and thermal analyses of high-performance magnetic shape memory actuators for valve applications," *IEEE Trans. Magn.*, vol. 52, no. 9, Sep. 2016, Art. no. 8205306.
[74] I. Goda, R. Rahouadj, J.-F. Ganghoffer, H. Kerdjoudj, and L. Siad, "3D couple-stress moduli of porous polymeric biomaterials using $\mu$CT image stack and FE characterization," *Int. J. Eng. Sci.*, vol. 100, pp. 25–44, Mar. 2016.
[75] S. B. Kochekseraii, "Effective conductivity of matrix composites and foam materials by self-consistent field method using commercial FEA software," *Int. J. Eng. Sci.*, vol. 98, pp. 110–115, Jan. 2016.
[76] R. Hashemi, "Magneto-electro-elastic properties of multiferroic composites containing periodic distribution of general multi-coated inhomogeneities," *Int. J. Eng. Sci.*, vol. 103, pp. 59–76, Jun. 2016.
[77] S. Kanaun, "Efficient homogenization techniques for elastic composites: Maxwell scheme vs. Effective field method," *Int. J. Eng. Sci.*, vol. 103, pp. 19–34, Jun. 2016.
[78] L. Alonso-González, S. Ver-Hoeye, M. Fernández-García, C. Vázquez-Antuña, and F. L.-H. Andrés, "From threads to smart textile: Parametric characterization and electromagnetic analysis of woven structures," *IEEE Access*, vol. 7, pp. 1486–1501, 2019.
[79] A. Abdelkefi, "Aeroelastic energy harvesting: A review," *Int. J. Eng. Sci.*, vol. 100, pp. 112–135, Mar. 2016.
[80] X. D. Xie, Q. Wang, and N. Wu, "A ring piezoelectric energy harvester excited by magnetic forces," *Int. J. Eng. Sci.*, vol. 77, pp. 71–78, Apr. 2014.
[81] M. Porfiri, F. dell'Isola, and F. M. F. Mascioli, "Circuit analog of a beam and its application to multimodal vibration damping, using piezoelectric transducers," *Int. J. Circuit Theory Appl.*, vol. 32, no. 4, pp. 167–198, 2004.
[82] M. Al Ahmad, A. M. Elshurafa, K. N. Salama, and H. N. Alshareef, "Modeling of MEMS piezoelectric energy harvesters using electromagnetic and power system theories," *Smart Mater. Struct.*, vol. 20, no. 8, 2011, Art. no. 085001.
[83] D. C. Hamill, "Lumped equivalent circuits of magnetic components: The gyrator-capacitor approach," *IEEE Trans. Power Electron.*, vol. 8, no. 2, pp. 97–103, Apr. 1993.
[84] N. Tran, M. H. Ghayesh, and M. Arjomandi, "Ambient vibration energy harvesters: A review on nonlinear techniques for performance enhancement," *Int. J. Eng. Sci.*, vol. 127, pp. 162–185, Jun. 2018.
[85] X. Tian, Q. Quan, L. Wang, and Q. Su, "An inchworm type piezoelectric actuator working in resonant state," *IEEE Access*, vol. 6, pp. 18975–18983, 2018.

**NIKITA GABDULLIN** (S'13–M'19) received the B.S. and M.S. degrees in electrical engineering from National Research University MPEI, Moscow, Russia, in 2010 and 2012, respectively, and the Ph.D. degree in electrical and electronic engineering from the City, University of London, London, U.K., in 2017. He is currently a Postdoctoral Researcher with Chung-Ang University, Seoul, South Korea.

His research interests include analytical and numerical modeling of electromagnetic fields, novel electrical machine design, multiphysics and coupled problem analysis, smart materials, and application of energy-efficient electromagnetic smart devices.

**JONG-SUK RO** received the B.S. degree in mechanical engineering from Han-Yang University, Seoul, South Korea, in 2001, and the Ph.D. degree in electrical engineering from Seoul National University (SNU), Seoul, in 2008.

He conducted research at the Research and Development Center of Samsung Electronics as a Senior Engineer from 2008 to 2012. From 2012 to 2013, he was with the Brain Korea 21 Information Technology of SNU, as a Postdoctoral Fellow. From 2013 to 2016, he was with the Brain Korea 21 Plus, SNU, as a BK Assistant Professor. He conducted research at the Electrical Energy Conversion System Research Division of the Korea Electrical Engineering and Science Research Institute, as a Researcher, in 2013. In 2014, he was with the University of BATH, Bath, U.K. He is currently an Assistant Professor with the School of Electrical and Electronics Engineering, Chung-Ang University, Seoul.

His research interest includes the analysis and optimal design of next-generation electrical machines.